การศึกษาเชิงทฤษฎีในการประยุกต์ใช้ท่อนาโนคาร์บอนเพื่อเป็นพาหนะในระบบนำส่งยาสู่เป้าหมาย

นางสาวชมพูนุช รุ่งนิ่ม

วิทยานิพนธ์นี้เป็นส่วนหนึ่งของการศึกษาตามหลักสูตรปริญญาวิทยาศาสตรดุษฎีบัณฑิต
สาขาวิชาวิทยาศาสตร์นาโนและเทคโนโลยี (สหสาขาวิชา)
บัณฑิตวิทยาลัย จุฬาลงกรณ์มหาวิทยาลัย
ปีการศึกษา 2555
ลิขสิทธิ์ของจุฬาลงกรณ์มหาวิทยาลัย

THEORETICAL STUDY ON THE USE OF CARBON NANOTUBE AS CARRIER FOR
TARGETED DRUG DELIVERY SYSTEM

Miss Chompoonut Rungnim

A Thesis Submitted in Partial Fulfillment of the Requirements
for the Degree of Doctor of Philosophy Program in Nanoscience and Technology
Interdisciplinary Graduate School
Chulalongkorn University
Academic Year 2012

Thesis Title	THEORETICAL STUDY ON THE USE OF CARBON NANOTUBE AS CARRIER FOR TARGETED DRUG DELIVERY SYSTEM
By	Miss Chompoonut Rungnim
Field of Study	Nanoscience and Technology
Thesis Advisor	Professor Supot Hannongbua, Dr. rer. nat.
Thesis Co-advisor	Associate Professor Vudhichai Parasuk, Ph.D.
Thesis Co-advisor	Thanyada Rungrotmongkol, Ph.D.

Accepted by the Faculty of Graduate School, Chulalongkorn University in Partial Fulfillment of the Requirements for the Doctoral Degree

....Dean of the Graduate School

(Associate Professor Amorn Petsom, Ph.D.)

THESIS COMMITTEE

....Chairman

(Assistant Professor Sukkaneste Tungasmita, Ph.D.)

....Thesis Advisor

(Professor Supot Hannongbua, Dr. rer. nat.)

....Thesis Co-advisor

(Associate Professor Vudhichai Parasuk, Ph.D.)

....Thesis Co-advisor

(Thanyada Rungrotmongkol, Ph.D.)

....Examiner

(Stephan T. Dubas, Ph.D.)

....Examiner

(Associate Professor Pornthep Sompornpisut, Ph.D.)

....External Examiner

(Professor Karl Peter Wolschann, Ph.D.)

ชมพูนุช รุ่งนิ่ม : การศึกษาเชิงทฤษฎีในการประยุกต์ใช้ท่อนาโนคาร์บอนเพื่อเป็นพาหนะในระบบ นำส่งยาสู่เป้าหมาย (THEORETICAL STUDY ON THE USE OF CARBON NANOTUBE AS CARRIER FOR TARGETED DRUG DELIVERY SYSTEM   อ. ที่ปรึกษาวิทยานิพนธ์หลัก: ศ. ดร. สุพจน์ หารหนองบัว, อ. ที่ปรึกษาวิทยานิพนธ์ร่วม: รศ.ดร. วุฒิชัย พาราสุข, อ.ดร. ธัญญดา รุ่งโรจน์ มงคล, 81 หน้า.

งานวิจัยนี้มีวัตถุประสงค์เพื่อทำความเข้าใจพฤติกรรมในระดับโมเลกุลของระบบนำส่งยาที่ใช้วัสดุ นาโนคาร์บอนเป็นพาหนะ เริ่มด้วยการเลือกแผ่นกราฟีนเป็นตัวแทนของโครงสร้างอะโรมาติกเพื่อศึกษา อันตรกิริยาระหว่างยารักษาโรคมะเร็งและวัสดุนาโนคาร์บอนด้วยทฤษฎีฟังก์ชันนัลความหนาแน่นและทฤษฎี ฟังก์ชันนัลความหนาแน่นชนิดยึดแน่น ผลการคำนวณพบว่าการยึดจับระหว่างยาและแผ่นกราฟีนถูกควบคุมด้วย อันตรกิริยาชนิด π-π ต่อมาทำการศึกษาความสามารถในการบรรจุยาแกมซิตาบีนภายในท่อนาโนคาร์บอนชนิด ผนังเดี่ยว (SWCNT) ด้วยการจำลองพลวัตเชิงโมเลกุล ซึ่งผลการศึกษาแสดงให้เห็นว่าภายในท่อนาโนคาร์บอน สามารถบรรจุยาได้มากกว่า 1 โมเลกุลโดยอาศัยอันตรกิริยาชนิด π-π ระหว่างวงอะโรมาติกของยาแกมซิตาบีนกับ ผนังด้านในของท่อนาโนคาร์บอนและแรงกระทำระหว่างโมเลกุลยาด้วยกันเอง จากนั้นทำการจำลองพลวัตเชิง โมเลกุลแบบเรพลิคาแอ๊กเชนจ์เพื่อศึกษาผลของความยาวของสายไคโตซาน (CS) ซึ่งทำหน้าที่เป็นวัสดุเชื่อมต่อ ระหว่างท่อนาโนคาร์บอนและโปรตีนควบคุมการเจริญเติบโต (EGF) พบว่าสายไคโตซานที่เหมาะสมควรมีค่า อัตราส่วนโดยมวลของไคโตซานและท่อนาโนคาร์บอนอย่างน้อย 1.26 เพื่อรักษาโครงสร้างของโปรตีน EGF และป้องกันความเกะกะของท่อนาโนคาร์บอนต่อบริเวณยึดจับระหว่างโปรตีน EGF และรีเซพเตอร์ (EGFR) นอกจากนี้ผลจากการจำลองพลวัตเชิงโมเลกุลได้ยืนยันว่าโปรตีน EGF ในระบบ EGF-CS-SWCNT มีความ สามารถในการยึดจับกับ EGFR ใกล้เคียงกับโปรตีน EGF ชนิดเดี่ยว โดยข้อมูลพื้นฐานของพฤติกรรมในระดับ โมเลกุลที่ได้จากงานวิจัยนี้มีประโยชน์ต่อการออกแบบและพัฒนาระบบนำส่งยาที่มีประสิทธิภาพสำหรับการ รักษาโรคมะเร็งต่อไปในอนาคต

ภาควิชา _____วิทยาศาสตร์นาโนและเทคโนโลยี ลายมือชื่อนิสิต _____

สาขาวิชา _____วิทยาศาสตร์นาโนและเทคโนโลยี ลายมือชื่อ อ.ที่ปรึกษาวิทยานิพนธ์หลัก _____

ปีการศึกษา _____2555_____ ลายมือชื่อ อ.ที่ปรึกษาวิทยานิพนธ์ร่วม _____

ลายมือชื่อ อ.ที่ปรึกษาวิทยานิพนธ์ร่วม _____

5287764820 : MAJOR NANOSCIENCE AND TECHNOLOGY
KEYWORDS: CARBON NANOTUBE / GRAPHENE/ DRUG DELIVERY SYSTEM

CHOMPOONUT RUNGNIM: THEORETICAL STUDY ON THE USE OF CARBON NANOTUBE AS CARRIER FOR TARGETED DRUG DELIVERY SYSTEM. ADVISOR: PROF. SUPOT HANNONGBUA, Dr. rer. nat., CO-ADIVISOR: ASSOC.PROF. VUDHICHAI PARASUK, Ph.D., THANYADA RUNGROTMONGKOL, Ph.D., 81 pp.

The objective of this research is to understand the behavior of drug delivery system (DDS) based on carbon nanomaterial at molecular level. Firstly, graphene sheets were selected as mimic models to study the binding interactions between anti-cancer drug and carbon nanomaterials by density functional theory (DFT) and density functional theory tight binding (DFTB). As suggested by the calculations, the drug-graphene bindings were mainly governed by π-π interactions. The loading capacity of gemcitabine drug inside single-walled carbon nanotube (SWCNT) cavity was subsequently studied by molecular dynamics (MD). The results showed that more than one anti-cancer drug can be encapsulated inside the tube cavity through the partial π-π stacking interaction between the aromatic cytosine ring of gemcitabine and the inner surface of the SWCNT together with the interactions among gemcitabine molecules themselves. Then, the effect of the length of chitosan (CS), an epidermal growth factor (EGF)-SWCNT linker, has been explored by replica exchange MD simulation. The appropriate chitosan length with a minimum mass ratio of chitosan per SWCNT of 1.26 can preserve EGF conformation and prevent the steric effect from SWCNT towards binding interface of EGF and its receptor, epidermal growth factor receptor (EGFR). Importantly, the EGF of EGF-CS-SWCNT had similar binding affinity with EGFR respect to the EGF alone as indicated from MD results. Taken together, these basic details of DDS behavior are helpful for the design and development of efficient device for cancer therapy in the near future.

Department: .... Nanoscience and Technology   Student's Signature ....

Field of Study: .... Nanoscience and Technology   Advisor's Signature ....

Academic Year: ..... 2012 ....   Co-advisor's Signature ....

                                                        Co-advisor's Signature ....

ACKNOWLEDGEMENTS

CONTENTS

LIST OF TABLES

LIST OF FIGURES

LIST OF ABBREVIATIONS

A	=	Adenine
C	=	Cytosine
cc-pVDZ	=	Dunning's correlation consistent with double zeta basis sets
cc-pVDZ	=	Dunning's correlation consistent with triple zeta basis sets
CCSD(T)	=	Coupled cluster single and doubles with perturbative triples
CNT	=	Carbon nanotube
CS	=	Chitosan
CYS	=	Cysteine
CYX	=	Cysteine with disulfide linkage
DDS	=	Drug delivery system
DFT	=	Density functional theory
DFTB	=	Density functional based tight binding
DFTB-D	=	Density functional based tight binding with dispersion correction
DFT-D	=	Density functional theory with dispersion correction
DOX	=	Doxorubicin
EGF	=	Epidermal growth factor
EGFR	=	Epidermal growth factor receptor
F	=	Fluorouracil
G	=	Guanine
GB	=	Generalized born
GC,GEMZA	=	Gemcitabine
GLS	=	D-glucosamine
HID	=	Histidine with hydrogen on the delta nitrogen
HIE	=	Histidine with hydrogen on the epsilon nitrogen
M06-2X	=	Parameterized meta-hybrid functional from Zhao Y.
MD	=	Molecular dynamics
MP	=	Mercaptopurine
MP2	=	Second order of Møller–Plesset perturbation theory
MWCNT	=	Multi-walled carbon nanotube

NAG	=	N-acetyl-D-glucosamine
PDB	=	Protein data bank
PEG	=	Polyethylene glycol
PL	=	Phospholipid
PM3	=	Parameterized Model number 3
REMD	=	Replica exchange molecular dynamics
RESP	=	Restrained electrostatic potential
SWCNT	=	Single-walled carbon nanotube
T	=	Thymine
TG	=	Thioguanine
U	=	Uracil
vdW	=	van der Waals
%DD	=	Degree of deacytylation of chitosan

CHAPTER I
INTRODUCTION

1.1 Drug delivery system (DDS)

At the present, DDSs, designed systems for the delivery drugs into diseased area with controllable drug releasing ability, have been mainly focused for cancer therapy because the number of patients continuously rises up every year and most of them are suffering from side effects of anti-cancer drugs in chemotherapy processes. [1] Basically, the DDS component consists of 3 main parts *i.e*., transporter, drug and medical device for targeting and releasing propose. Nowadays, there are many types of materials that can be used as carrier in DDS such as liposomes, microspheres, biopolymers and nanoparticles. In the present study, carbon nanomaterials *e.g*., carbon nanotube (CNT) and graphene, are chosen as models for drug carriers due to their useful and unique properties such as high surface area, high thermal conductivity, and abilities to be functionalize with guest molecules.

1.2 Graphene

Graphene is a single layered sheet of polycyclic aromatic hydrocarbon and considered as 2D dimensional carbon nanomaterials. Even it was first discovered in 2004 [2], the unique physical, electronic and chemical properties of graphene have attracted attentions from various research areas. In biomedical applications, its high surface area with large π-aromatic system is proper for binding of biomolecules such as biopolymers, nucleobases [3], amino acids, DNA [4,5], RNA and aromatic anti-cancer drugs [6]. Besides, it was found that functionalized graphene can protect DNA from enzymatic cleavage during cellular delivery [7]. Although graphene is one of successful candidates as drug delivery vehicle, the understanding of interaction between guest

molecules and the sheet is still needed. In theoretical study, the mimic planar aromatic molecules of graphene sheet, *i.e*., coronene ($C_{24}H_{12}$), circumcoronene ($C_{54}H_{18}$) and circumcircumcoronene ($C_{96}H_{24}$), as shown in Fig. 1.1, have been used as models for guest molecule adsorption to investigate the intermolecular interaction between the guest molecule and graphene. [8,9]

Coronene
($C_{24}H_{12}$)

Circumcoronene
($C_{54}H_{18}$)

Circumcircumcoronene
($C_{96}H_{24}$)
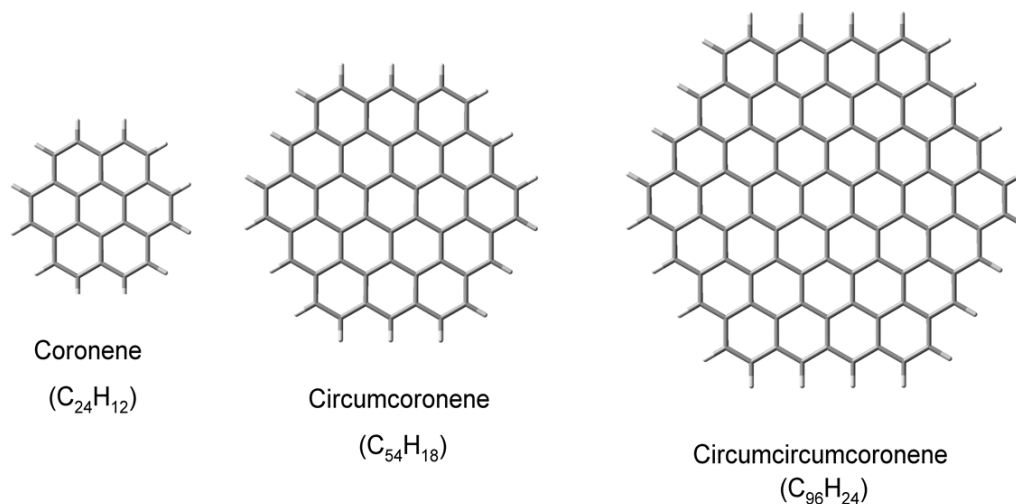
Figure 1.1 Structural Geometries of coronene ($C_{24}H_{12}$), circumcoronene ($C_{54}H_{18}$) and circumcircumcoronene ($C_{96}H_{24}$)

1.3 Carbon nanotube

Carbon nanotubes (CNTs) discovered by Iijima and coworkers in 1991 [10] are divided into two types, single-walled carbon nanotubes (SWCNTs) and multi-walled carbon nanotubes (MWCNTs). SWCNTs can be imaged as long wrapped single graphene sheet while MWCNTs are considered as a group of concentric SWCNTs with different diameters as shown in Fig. 1.2. Types of SWCNT are classified from how graphene sheet-rolls to cylinder tube as represented by (*n,m*) lattice vector. The (*n,m*) indice also determines the diameter and the chirality of SWCNT. The tubes with (*n,0*) lattice vector are defined as zig-zag SWCNTs, while the (*n,n*) tubes are named for armchair SWCNTs and other tubes are called chiral SWCNTs [11,12] as shown in Fig.

1.2. The electronic properties of SWCNTs strongly depend on their symmetry, *e.g,* the (n,m) SWCNTs are metallic when $n = m$ or $n - m$ is a multiple of 3. Otherwise they are considered as moderate semiconductors [13,14].
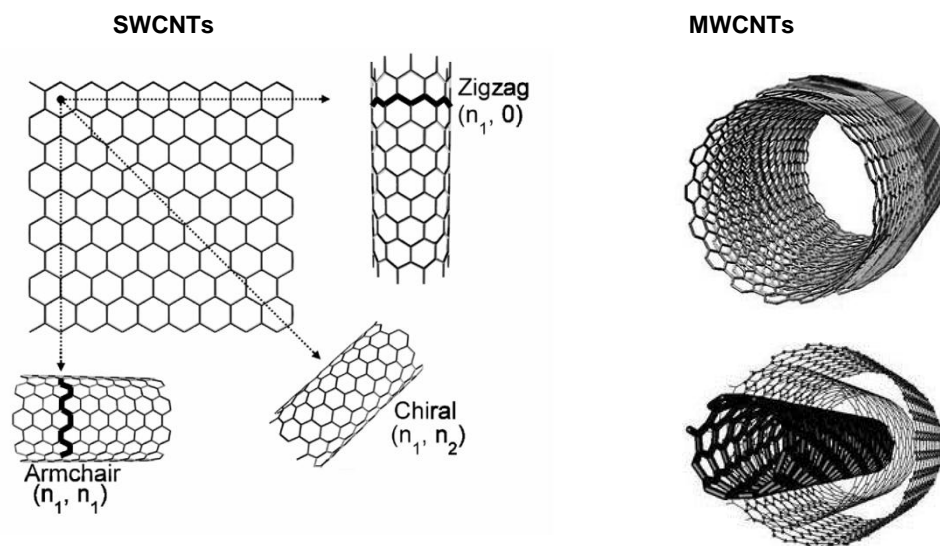
Figure 1.2 The schematic views for SWCNTs with armchair, zigzag and chiral structures and MWCNTs. [15]

Due to high hydrophobicity, CNTs are very low dispersion in aqueous solutions. To enhance water solubility and biocompatibility, their surfaces should be functionalized or by hydrophilic molecules or biopolymers, such as chitosan, alginate, polyethylene glycol (PEG), phospholipid (PL), phospholipid-poly(ethylene glycol) (PL-PEG) [16] and pyrene-PEG [17].
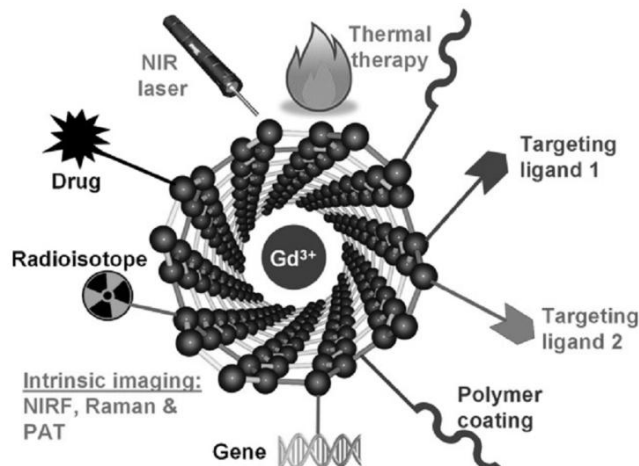
Figure 1.3 A multifunctional SWCNT-based platform incorporates with targeting ligands, therapeutic agents (drug and gene), biocompatibility agent (biopolymer) and specific function for imaging and thermal therapy [18].

The high surface area and large aromatic conjugation of CNTs cavity are appropriate for molecule adsorption on both inside and outside the surfaces. Moreover, CNTs are also alternative and efficient tools for DDS because they offer possibilities to be functionalize with more than one kind of guest molecules for each specific propose on the same tube as depicted in Fig. 1.3. Recently, many researches have reported the succes of DDS based on CNT. [19-23] For example, the encapsulation of cisplatin anti-cancer agent inside the oxidized SWCNTs network was effective in reducing the growth of human lung-cancer cell by slowly releasing cisplatin to the target cell [24]. Besides, doxorubicin anti-cancer drug can be loaded onto PEG functionalized SWCNTs using supramolecular π-π stacking between doxorubicin and SWCNT surface [25]. The further details on anti-cancer drug and surface modification agent will be discussed.

1.4 Anti-cancer drug

The anti-cancer drugs are normally designed to stop or slow down the growth and spread of cancer cell divisions by interrupting and damaging DNA synthesis or stop mitosis in cell division process [26]. For that reason, some anti-cancer drugs have similar structure to nucleobases, as can be seen in Fig. 1.4. The structures of the four anti-cancer drugs and their analog nucleobases are shown in Fig. 1.4. Non-covalent interactions between graphene and these guest molecules were proposed to involve with dispersion interaction. Computational techniques have been applied to understand the dispersion interactions in the adsorptions of nucleobases, (A, C, G, T and U) over graphene. [7-13] For example, interaction energies of stacked graphene-nucleobase complexes at quantum chemical method that include dispersion interactions, DFT-D methods, confirmed that dispersion interaction strongly influences to the interaction between graphene and nucleobases and sequence of the interaction energy was in the order of G > A > T > C > U. [14] In addition, semi-empirical approach PM3 with dispersive correction provides considerable accuracy and cost effective to computing the interaction energy of nucleic acids with graphene compared with more time consuming DFT-D and MP2 methods [9]. Besides analogue anti-cancer drugs, there are also some antibiotics with anti-cancer activity that are important and widely applied in several cancers treatment, such as daunorubicin and doxorubicin. Recently, doxorubicin has been chosen as model of anti-cancer drug in many DDSs based on CNTs. [25,27-29] It has been proposed that doxorubicin can be bound to CNT surface via π-π interaction as confirmed by the results from theoretical study [30]. However, there are not sufficient details known about the interaction between drugs and graphene which should be useful to provide basic information and to increase the understanding of the π-π interaction of drugs and carbon nanomaterial carrier.
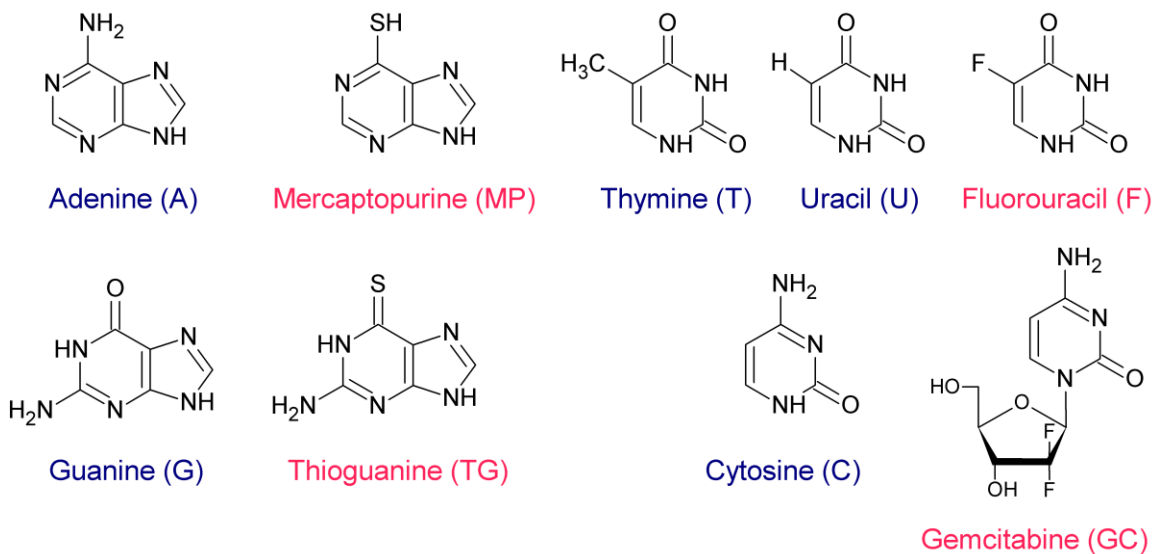
Figure 1.4 Structural geometries of nucleobases (A, G, C, T and U) and their analog anti-cancer drugs (MP, TG, GC and F).

1.5 Chitosan

Chitosan (CS) is a biopolymer resulted from deacetylation reaction of N-acetyl gulcosamine (NAG) in chitin polymer chain. The number of deacetylated unit, glucosamine (GLS), in chitosan is reported as degree of deacytylation (%DD). Recently, chitosan has been used as biocompatible agent and linker to combined bimolecular agent with drug carrier in many DDS applications because of its outstanding biocompatibility and low toxicity [31-35]. The wrapping of chitosan over CNTs surface was also reported to improves the dispersion as well as biocompatibility of the tubes confirmed by both experimental and theoretical studies in which the %DD of 60 was reported to be the lowest %DD that significantly enhanced dispersion of SWCNTs. [36,37]

Glucosamine, R= H

N-acetylglucosamine, R= COCH$_3$
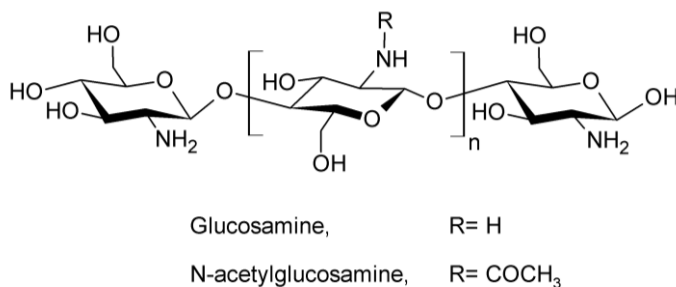
Figure 1.5 Chemical structures of chitosan chain consisting of two monomers, glucosamine (GCS, R=H) and N-acetylglucosamine (NAG, R=COCH$_3$).

1.6 Targeting agent to cancer cell

Most of anti-cancer drugs are designed to kill or to stop the growth of cancer cells. Therefore, the anti-cancer drugs are also toxic to quickly growing of normal cells such as cells in the intestinal, hair and bone marrow areas. To reduce these side effects, the DDS specificity should be improved. From the fact that the growth and cell division rate of cancer cells are abnormally faster than those of most normal cells, so, cancer cells have high levels of key growth factor receptors, such as the folic acid receptor and epidermal growth factor receptor (EGFR) [38-40]. EGFR is a member of tyrosine kinase receptors that consists of many flexible parts, *i.e.*, a large extracellular ligand binding region, a single transmembrane domain and an intracellular tyrosine kinase domain [41]. The extracellular region of EGFR is divided into four domains named domain I, II, III and IV [42-44]. In domain I (residue 1-165) and III (residue 310-481), their amino acids chain fold into single stranded right-handed β-helical barrels and the two domains contribute to ligand binding [45]. The cysteine-rich domains, domain II (residue 166-309) and IV (residue 482-618), contain small disulfide bonds which construct the chain protein into an extended rod-like structure. The interaction of this extended beta-hairpin loop in domain II with a pocket in domain IV prevents the close contact between domain I and III which is proper

for the approach of ligand binding. This auto-inhibit conformation of EGFR is called tether or inactive form. The activation of tyrosine kinase at intracellular region of EGFR was proposed to trigger from dimerization of EGFR.[46,47] For that reason, dimer of EGFR is known as active form. Many study confirmed that the binding of EGF with domain I and III of EGFR induce the rearrangement of domain II and IV to proceed the dimerization process of EGFR and activate tyrosine kinase activities that control proliferation, motility and differentiation of the cell [41,43-45,48-50] as shown in Fig. 1.6.
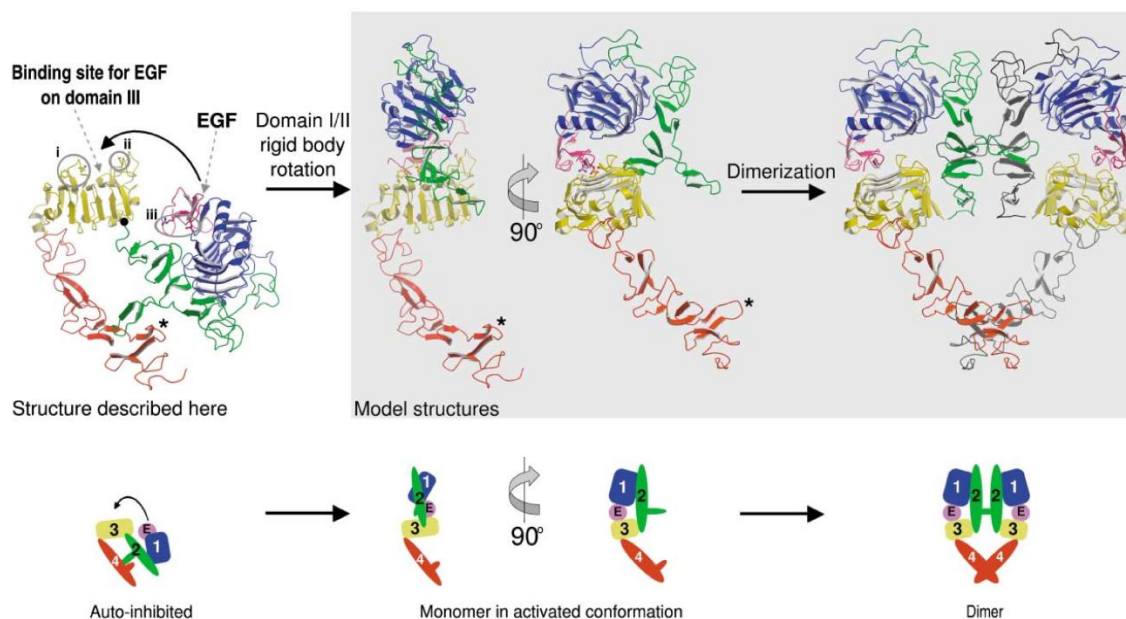
Figure 1.6 The model of ligand induced dimerization of EGFR [44]

Hence, ligands with high affinity to these receptors such as epidermal growth factor (EGF) [51-54] can be used as specific targeting agents to cancer cells, shown as schematic view in Fig. 1.7. For example, the *in vitro* study of oxidized SWCNTs conjugated with EGF and cisplatin anti-cancer confirms that EGF can be used as targeting agent to increase specificity of DDS to cancer cell shown as rapid decreasing of tumor size and specific localization of DDS to the cancer cell area. [55] Although many studies confirm the success of EGF-CNT based drug

delivery, there is a small number of research groups focusing on the intermolecular interactions between EGFR and the bioconjugated CNT (EGF-CNT).
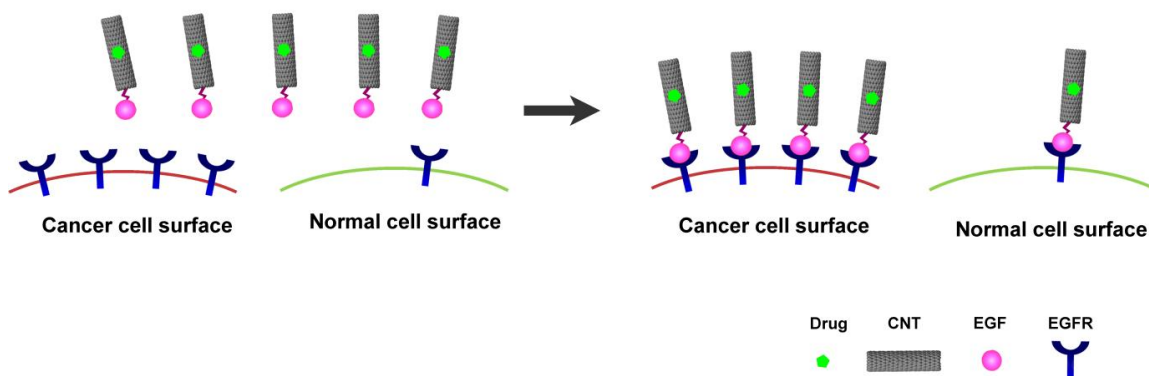
Figure 1.6 Schematic process of carbon nanotube for selective recognition and targeted drug delivery system.

According to all above informations, although are many experimental studies have reported the success of graphene and CNT as anti-cancer drug carrier in DDS, further details about interactions among DDS components and the interactions between DDS and cancer cell receptor protein are required to fulfill the understanding of the DDS. For that reason, the aim of the present study is to provide molecular properties of targeted DDS by using computation chemistry techniques. The study content is divided in to 5 parts as shown below;

1. The non-covalent interaction of nucleic acid analogue anti-cancer drug with graphene

2. Investigation of the arrangement of doxorubicin over graphene

3. Gemcitabine anti-cancer drug loading capacity on carbon nanotube

4. The effect from length of chitosan linker to the conformation of EGF in targeted DDS

5. Binding interaction of targeted DDS with EGFR of cancer cell

CHAPTER II
THEORY

2.1 Density functional theory (DFT)

In density functional theory (DFT), the total energy and properties of a molecular system can be determined from the electron density (ρ). The concept of density functional theory comes from Thomas-Fermi model [56] and later proven by Hohenberg and Kohn [57] in 1964. In the DFT theory, the total energy is written as

$$E[\rho] = T[\rho] + V_{ext}[\rho] + V_{ee}[\rho] \tag{2.1}$$

where $T[\rho]$ is kinetic energy, V_{ext} is the interaction with external potential and V_{ee} is the electron-electron interaction.

Kohn-Sham proposed non interaction electrons to appproximate the kinetic energy and electron-electron function as

$$T_S = -\frac{1}{2}\sum_{i=1}^{N}\langle\varphi_i|\nabla^2|\varphi_i\rangle \tag{2.2}$$

The electron-electron interaction was noted as classical Coulomb interaction, $J[\rho]$,

$$J[\rho] = \frac{1}{2}\iint \frac{\rho(r)\rho(r')}{|r - r'|}\,drdr' \tag{2.3}$$

Thus, the energy function of Kohn-Sham equation can be written as,

$$E[\rho] = T_S[\rho] + V_{ext}[\rho] + J[\rho] + E_{xc}[\rho] \tag{2.4}$$

where the exchange-correlation functional, E_{xc}, is the summation of the error from non-interacting kinetic energy and the error made in treating electron-electron interaction defined as,

$$E_{xc}[\rho] = (T[\rho] - T_S[\rho]) + (V_{ee}[\rho] - J[\rho]) \tag{2.5}$$

According Schrödinger's equation, the resulting equations of Kohn-Sham equation for one-electron equation is

$$\left(-\frac{1}{2}\nabla^2 + V_{eff}(r)\right)\psi_i = \varepsilon_i\psi_i \tag{2.6}$$

where $V_{eff}(r)$ is

$$V_{eff}(r) = V(r) + \frac{\delta J}{\delta\rho} + \frac{E_{xc}}{\delta\rho} \tag{2.7}$$

$$V_{eff}(r) = V(r) + \frac{1}{2}\int\frac{\rho(r')}{|r-r'|}dr' + V_{xc} \tag{2.8}$$

Due to the exact functional of exchange-correlation term are unknown, for that reason, approximations were applied to the exchange-correlation function such as local-density approximation (LDA), generalized gradient approximation (GGA), hybrid GGA and meta hybrid GGA.

The dispersion interaction and van der Waals (vdW) forces are important interactions in many compounds such as DNA, proteins and carbon nanomaterials. Many researchers have been focused to improve the accuracy of the calculation in DFT method. One of the deficiencies of DFT calculation is the lack of the dispersion energy. The review from Grimme [58] shows that there are several methods to increase the dispersion correction accuracy as shown in Fig. 2.1. The vdW-DF is a non-empirical method to compute the dispersion energy by adding dispersion energy term in Kohn-Sham equation. The parameterized DF is modified by parameterizing the standard meta-hybrid approximation *e.g.* M05 and M06 family of functionals. [59,60] The DFT-D method is a semi-classical correction by summation of pairwise atom over C_6R^{-6} potential. The

last dispersion-correction method, dispersion-correcting atom-centered one-electron potential (DCACP), is based on the concept of one-electron correction potential.
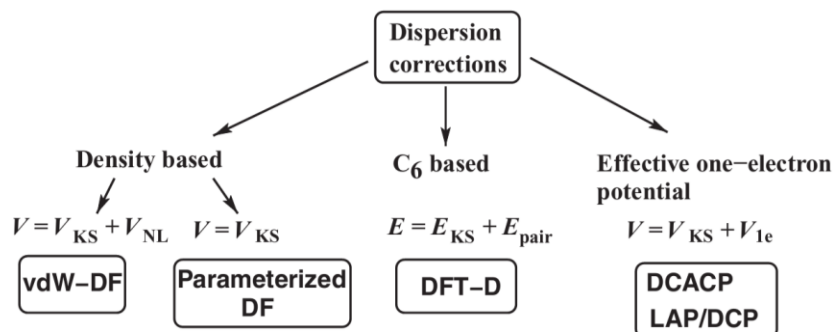
Figure 2.1 The currently dispersion correction in DFT (E_{KS} and V_{KS} are Kohn-Sham total energy and potential, respectively [58].

2.2 Density functional tight binding (DFTB) theory

To speed up the calculation and offer the possibility to study with the systems contained higher than 100 atoms, semi-empirical methods were applied. The density functional tight binding (DFTB) method is one of the recognized approximate DFT. The DFTB contains following approximations:

1) Density and potential functions are written as superposition of atomic density and potentials

2) The many-body Hamiltonian in DFT is replaced with parameterized Hamiltonian matrix by summarize with repulsion energies and written as a summation of pairwise repulsive terms.

3) The Kohn-Sham orbitals are expended in a set of localized atom centered function (LCAO) and written in term of Slater-type orbitals where Hamiltonian and overlap matrices contain only one- and two-center contribution.

The general DFTB can be obtained from

$$E_{tot}^{DFTB} = \sum_{i}^{\substack{\text{valence} \\ \text{orbitals}}} n_i \, \varepsilon_i + \frac{1}{2}\sum_{\alpha\beta}^{N} E_{rep}^{\alpha\beta} \tag{2.9}$$

where n_i and ε_i are occupation and orbital energy of the Kohn-Sham eigenstate and E_{rep} corresponds to a sum of short-rang repulsive potentials.

To describe the charge-transfer phenomenon property, induced-charges term which determined from Mullikan population analysis is included. The obtained solution is named self-consistent charge density functional tight binding (SCC-DFTB). The SCC-DFTB total energy is obtained from

$$E_{tot}^{SCC-DFTB} = \sum_{i}^{\substack{\text{valence} \\ \text{orbitals}}} n_i \, \varepsilon_i + \frac{1}{2}\sum_{\alpha\beta}^{N} \gamma_{\alpha\beta} \, \Delta q_\alpha \Delta q_\beta + \frac{1}{2}\sum_{\alpha\beta}^{N} E_{rep} \tag{2.10}$$

where the first term is energy summation over all occupied eigenstate, the second term is derived from second-order expansion of the exchange-correlation functional respected to the charge density fluctuation which approximated as atomic charge (Δq) and the last term, E_{rep}, corresponds to a sum of short-rang repulsive potentials.

Additionally, the dispersion energy ($E_{disp,}$) can be included into the DFTB approach and named DFTB-D as shown in Eq. 2.11.

$$E_{tot}^{DFTB-D} = E_{DFTB} + \sum_{i<j} E_{dispersion} \, (i,j) \tag{2.11}$$

The dispersion term is determined as,

$$E_{dispersion} = -\sum_{i<j} f_{ij}\left(R_{ij}\right) \frac{C_6^{ij}}{R_{ij}^6} \tag{2.12}$$

where R_{ij} is interatomic distance, C_6^{ij} is dispersion coefficient for ij atom pair and $f_{ij}(R_{ij})$ is a damping function to switch off the calculation for atoms with distances shorter than a characteristic distance of chemical bonding region, R_o.

$$f_{ij}(R_{ij}) = \begin{cases} \approx 1, & R \geq R_o \\ \approx 0, & R \leq R_{o,} \end{cases} \tag{2.13}$$

2.3 Molecular dynamics simulation

Molecular dynamics (MD) simulation based on Newton's second law is a helpful technique to simulating the time dependent behavior of systems because molecular activities come from the time dependent interactions between molecules at atomic level. The MD can provide information at the microscopic level, *e.g.*, atomic positions, velocities and atomic energies. This microscopic information is then converted to the macroscopic level, *e.g.*, pressure, temperature, heat capacity and stress tensor by using statistical mechanics. The concept of the statistic mechanics is based on Gibbs ensemble where the term "ensemble" is a collection of all possible systems having different microscopic states but identical macroscopic or thermodynamics states. One fundamental ensemble is called the micro-canonical ensemble and is categorized by constant particle number (N), constant volume (V) and constant total energy (E), denoted as the NVE ensemble. Other examples are the canonical or NVT ensemble, the isothermal-isobaric or NPT ensemble, and the grand-canonical or μVT ensemble [61].

The essential parameters for classical MD simulation are (i) potential energy of particles to calculate the forces, and (ii) the equation of motion governing the dynamics of the particles.

From Newton's law,

$$F_i = m_i a_i \tag{2.14}$$

Where F_i, m_i and a_i are force, mass and acceleration of particle i, respectively. The force can be expressed as the gradient of the potential energy (V),

$$F_i = -\nabla_i V \tag{2.15}$$

Combining (2.14) and (2.15) together are obtains,

$$-\frac{dV}{dr_i} = m_i \frac{d^2 r_i}{dx^2} \tag{2,16}$$

From equation (2.16), Newton's equation of motion can then related to the potential energy and the changes of position as a function of times. If atomic forces and masses are obtained, then the positions of each atom along a series of extremely small time steps (on the order of femtoseconds) can be solved.

Basically, the total potential energy of a system can be derived from simply physical forces,

$$V = E_{bonded} + E_{non-bonded} \tag{2.17}$$

where $$E_{bonded} = E_{bond} + E_{angle} + E_{torsion} \tag{2.18}$$

$$E_{non-bonded} = E_{van\ der\ Waals} + E_{electrostatic} \tag{2.19}$$

For bonded term, the E_{bond} term is applied from the concept from Hook's Law. The E_{angle} term describes the energy change associated with deviation from an ideal bond angle geometry while $E_{torsion}$ term describes the energy associated with the rotation of dihedral angle around the middle bond. For the non-bonded term, the van der Waals interaction is obtained from Lennard-Jones potential in Eq. (2.20), while Coulomb potential is applied for the electrostatic term as shown in Eq. (2.21).

$$V(r)^{LJ} = 4\epsilon \left[\left(\frac{\sigma}{r} \right)^{12} - \left(\frac{\sigma}{r} \right)^6 \right] \tag{2.20}$$

where ϵ is the cohesive energy well depth, σ is the equilibrium distance and r represent the distance between particles.

$$V_{ele} = \frac{q_i q_j}{\varepsilon \, r_{ij}} \tag{2.21}$$

where r represents the distance between two atoms having the charges q_i and q_j, while ε is the effective dielectric function

Due to the fact that the potential energy is a function of all atoms in the system, the numerical algorithms have been applied for integrating the equation of motion such as Verlet algorithm, Leap-frog algorithm, Velocity Verlet, Beeman's algorithm and symplectic reversible integrators. Generally, all algorithms assume the position, velocities and acceleration by Taylor series expression to predict the system configuration at time $(t + \delta t)$. To summarize the procedure, at each step, the forces on the atoms are computed and combined with the current positions and velocities to generate new positions and velocities a short time ahead. The force acting on each atom is assumed to be constant during the time interval. The atoms are then moved to the new positions, an updated set of forces is computed and new dynamics cycle goes on.

2.4 Replica exchange molecular dynamics simulation

Since most of MD simulation studies are relied on canonical ensemble simulations, the problem of many local minima traps cause a limit range of sampling and lead to incorrect results. Increasing the simulation temperature can rise up the probability to cross the barrier from one minimum to another and result in higher probability to achieve the global minimum.

Replica exchange molecular dynamics (REMD) simulations is applied to solve this problem [62-67]. Generally, REMD is the set of several independent simulations run at different temperatures in parallel and attempt to exchange temperatures of any two neighbor replicas with probability of

$$w(X \rightarrow X') = \begin{cases} 1, & for \quad \Delta \leq 0 \\ \exp(-\Delta), & for \quad \Delta > 0 \end{cases} \tag{2.22}$$

where $\Delta = \left[\frac{1}{kT_1} - \frac{1}{kT_2}\right](E_2 - E_1)$

If the difference of temperatures $(T_2$-$T_1)$ of the two replicas is small enough and their energies are overlapping, then the exchange of temperature between the two replicas is allowed otherwise the exchange is rejected and each replica is simulated at the previous temperature, shown in a schematic view in Fig. 2.1.
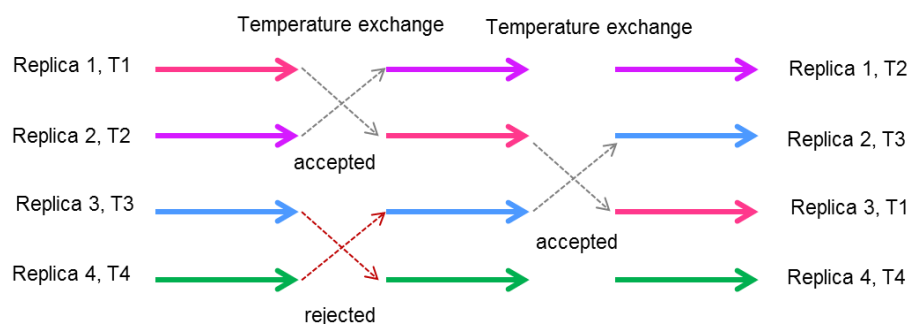
Figure 2.2 Schematic view of REMD simulation

The exchanges of temperature following the criteria as Eq. 2.9 enhance random walks from local minima to other minima and may reach global minimum of potential energy surface. For example, the comparison of results from two single canonical MD simulation at T=200 and 700 K with REMD simulation (8 replicas in the temperature range of 200 - 700 K) of Gly-2 by Sugita [62] shows that REMD simulation give broader configuration (Fig. 2.2b) than

conventional canonical simulation (Fig.2.2a) even at low temperature (200K). The lower probabilities of the position observed from canonical simulation in the result of REMD imply that the simulation at low temperature of canonical simulation is trapped in one of the local minima state. For that reason, REMD is a useful method for investigate the configuration of systems with high-dimensional rough energy surface like proteins.
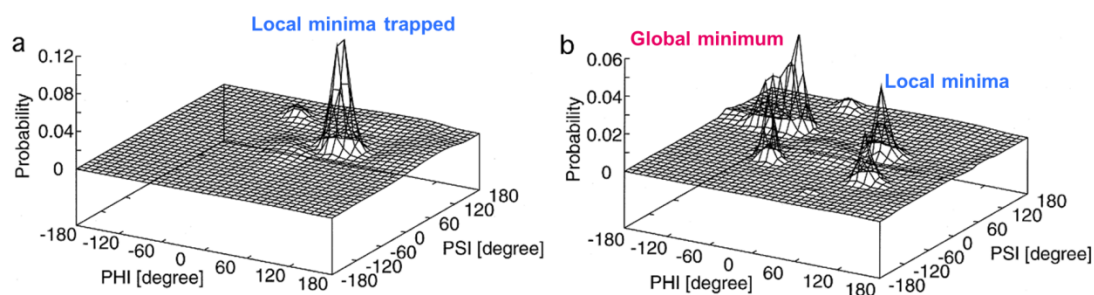
Figure 2.3 Distributions of dihedral angles of Gly-2: (a) from a regular canonical MD simulation at 200 K, (b) from the replica-exchange MD simulation at T=200 K [62].

CHAPTER III

METHODOLOGY

3.1 The non-covalent interaction of nucleic base analogue anti-cancer drug with graphene

First of all, the binding interactions of benzene dimer were calculated with M06-2X, MP2, and CCSD(T) methods to understand the basic concept of dispersion interaction from aromatic compounds. After that, complexes of graphene with nucleobases (A, C, G, T and U) and nucleic base analogue anti-cancer drugs (MP, GC, TG and F) were created and calculated their binding energies by using Gaussian 09 software to describe the non-covalent interaction as well as the dispersion interaction between the guest molecules and graphene.
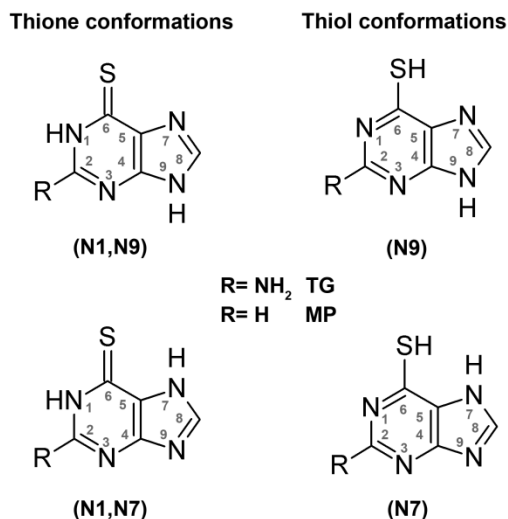
Figure 3.1. Tautomeric conformations of MP and TG. [68-70]

In case of purine base analogue, MP and TG, many tautomer conformations have been reported as shown in the Fig. 3.1. From theoretical calculation, TG(N1,N9) is the most stable thione tautomer of TG in gas phase while those of MP is the thiol conformation in MP(N9). [68,70] For that reason, the most stable structure in gas phase of MP and TG were chosen in the present study.

3.2 Investigation of the orientation of doxorubicin over graphene

The alignment of neutral and positive charged doxorubicin over graphene were investigated by using density functional based tight binding (DFTB)[71]. The aromatic conjugation of graphene was represented by graphene sheet $C_{216}H_{36}$ created by using material studio software package while the structure of doxorubicin obtained from Drug Data Bank Database (entry code: DB00997) [72]. To generate various orientation of doxorubicin over graphene sheet, the private code developed from Prof. Stephan Irle's group were applied on the system to obtain 500 complexes with difference in doxorubicin orientation. After that, all 500 complexes were fully optimization using DFTB method with dispersion correction (DFTB-D) [73] in DFTB+ 1.2 software. [74] Then, all the optimized structures were examined in terms of energy decomposition and structural analysis to overlook the energy surface of doxorubicin-graphene complex. The same procedure was applied to generated 500 orientations of positively charged doxorubicin over graphene to compare the effect of positive charge of the drug to the binding with graphene. In the analysis part, the distances between heteroatoms and graphene were measured. The interaction energies, E_{INT}, between drug and graphene were calculated by using Eq. (3.1).

$$E_{INT} = E_{complex} - E_{graphene} - E_{drug} \qquad (3.1)$$

All geometry optimizations as well as frequency calculation were performed with meta-hybrid DFT functionals, M06-2X, in conjugated with correlation-consistent polarized basis sets such as cc-pVDZ and cc-pVTZ. In addition, counterpoise corrections were applied to eliminate basis set superposition error (BSSE). The obtained interaction energies of each nucleic acid and analogue anti-cancer drug were compared at 3 difference sizes of graphene sheets, coronene ($C_{24}H_{12}$), circumcoronene ($C_{54}H_{18}$) and circumcircumcoronene ($C_{96}H_{24}$) to evaluate the edge effect of the sheet and the influence of the graphene size to the non-covalent interaction. Moreover, the achieved results were also compared with other DFT methods, such as DFT-D, that can explain dispersion interactions and van der Waals (vdW) interactions of aromatic molecules.

3.3 Gemcitabine anti-cancer drug loading capacity of carbon nanotube

Preparation of the initial structures
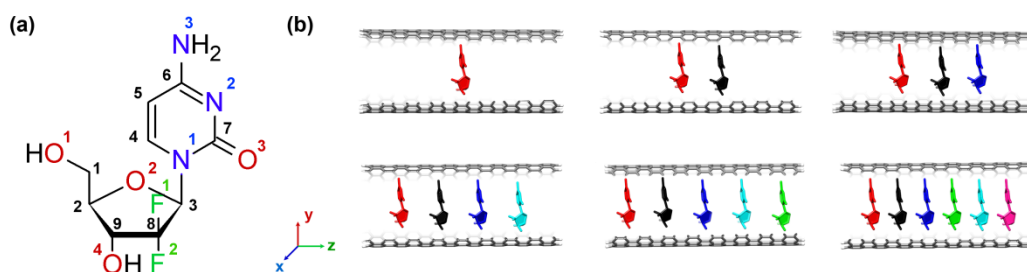
Figure 3.2 (a) Chemical structure of the anti-cancer drug, gemcitabine, with atomic labels. (b) Initial structure of the six studied systems with different drug loadings (1-6 gemcitabine molecules per SWCNT) contained inside the SWCNT cavity where the x-, y- and z- axes are also assigned.

To investigate the molecular properties of different drug loadings inside the SWCNT, (18,0) open-ended SWCNT with a 14 Å diameter and 34 Å length were selected as DDS model in this study. The six systems with different uptakes of gemcitabine in the SWCNT cavity were generated by increasing the number of drug molecules from 1 to 6 labeled as i-GEMZAR, where i = 1-6, respectively. The gemcitabine geometry (atomic labels of the drug are shown in Fig. 3.2a) was extracted from the co-crystal structure of human deoxycytidine kinase bound to gemcitabine (PDB code 2NO0). [75] In the initial state, the gemcitabine molecules of all drug-SWCNT complexes were placed in the middle of the SWCNT with equivalent inter-molecular distances between each drug molecule when more than one was present, as illustrated in Fig. 3.2b. Afterwards, each complex was solvated with the SPC/E water model in an octagonal box over 12 Å from system surface. In all simulations, parameter for CA atom type from AMBER03 force fields [76] were applied for the SWCNT [36], while the atomic charges and parameters of gemcitabine were taken from reported calculations of Uthumporn *et.al* [77].

MD simulations setup

All MD simulations were carried out under the periodic boundary condition with the NPT ensemble at 1 atm and 300 K using the SANDER module of the AMBER 10 program package by using standard procedures [13,78,79]. The SHAKE algorithm [80] was applied to all covalent bonds involving hydrogen atoms. A time step of 2 fs and a cutoff function at 12 Å for non-bonded interactions were used for all systems. The long-range electrostatic interactions were calculated via the particle mesh Ewald Sum method [81]. Afterwards, each system was heated up to 300 K for 60 ps, and then fully unrestrained MD simulations were performed for 20 ns. The trajectories extracted every 1 ps from the last 10 ns were used for all analyses.

3.4 The effect from length of chitosan linker to the conformation of EGF in targeted DDS
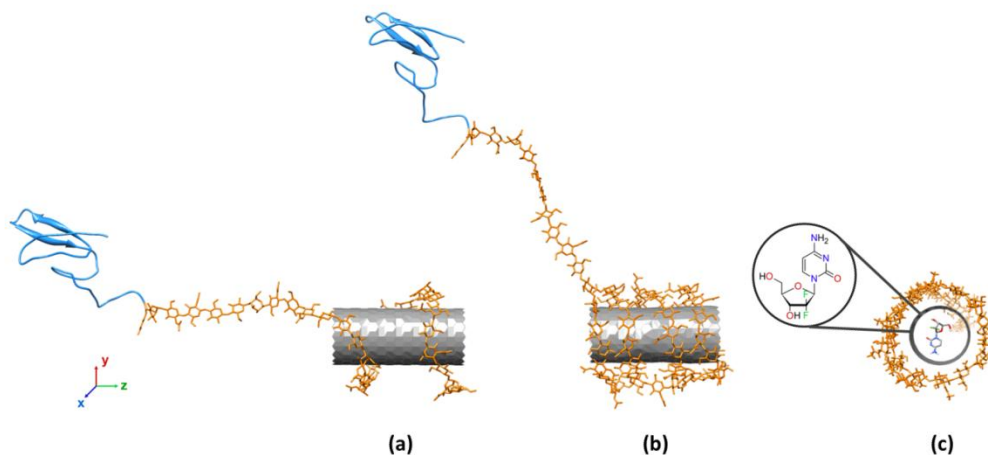
Figure 3.3 Schematic view of the initial DDS structure of (a) the EGF/30CS/SWCNT/Gemzar and (b) the EGF/60CS/SWCNT/Gemzar DDSs. EGF is represented as a blue ribbon and the chitosan units are shown as an orange line wrapped around the SWCNT (grey surface). Gemcitabine is located inside the SWCNT cavity as seen in (c) the cross-section view of the SWCNT.

Preparation of the initial structures

In this part, two DDSs composed of four components; SWCNT, EGF, chitosan of two different chain lengths (30CS and 60CS) and gemcitabine (Gemzar) termed as EGF/30CS/SWCNT/Gemzar and EGF/60CS/SWCNT/Gemzar, respectively, were generated. The EGF and gemcitabine structures were obtained from PDB entry codes INQL [44] and 2NO0 [75], respectively. The 30CS and 60CS chains were helically wrapped on (18,0) zig-zag SWCNT with 14 Å in diameter and 34 Å in length using the Material Studio 4.3 package software. Both the 30CS and 60CS chains had a 60% degree of deacetylation (%DD) in a random sequence of NAG

and GLS monomers. The 60% DD level was selected because it is the lowest %DD that significantly improved dispersion of SWCNTs [37]. The 30CS chain composed of 12 NAG and 18 GLS, whilst the 60CS chain composed of 24 NAG and 36 GLS units. To create the complex systems, EGF was covalently linked to the chitosan chain via a peptide bond between the backbone carbonyl carbon of R53 at the C terminal end of EGF and the nitrogen of the first chitosan unit. Additionally, the gemcitabine drug was placed inside the center of the SWCNT cavity, as shown in Fig. 3.3 where the initial structures of the two systems were also illustrated. The molecular topologies of the two systems were produced using antechamber tools in AMBER10 software [13,78,79]. The parameters of EGF and SWCNT were applied using AMBER03 force field [76], while GLYCAM06 force field was govern for chitosan [82]. The partial charges and parameters of gemcitabine were applied as in previous sessions [77].

REMD simulations setup

The calculations of the two DDSs were performed using AMBER10 software package. Firstly, all systems were minimized with steepest descent of 2500 steps. Then, the minimized structures were applied to REMD simulations over a temperature range of 300-455 K. After that, 32 replicas with the difference in the temperature between each replica of 5 K were set to obtain acceptance ratio in the range of 20-50% probability. Afterward, equilibration at each temperature was simulated for 20 ps. Then, equilibrated structure at each temperature was the starting conformation for each replica in REMD simulation. The simulations were performed for 5 ns where the replica exchanges were attempted every 1 ps and the trajectories were written every 2 ps.

3.5 Binding interaction of targeted DDS with EGFR of cancer cell

Preparation of the initial structures

To explore the binding of EGF and EGFR with and without the presence of DDS, 2 complexes of EGFR with different functionalized EGF were generated. The first system was the binding of EGFR with pristine EGF (EGFR•EGF). The other system was complexes of EGFR bounded with EGF linked with SWCNT through a wrapped chitosan chain, entitled as EGFR•EGF-CS-SWCNT-Drug, respectively.

For the first system, EGFR•EGF, the structural geometry was obtained from crystallographic structures of EGF and extracellular region of EGFR in the Protein Data Bank (PDB) codes 1NQL [44] where number of residues of EGFR and EGF are 612 and 53 amino acids, respectively. The missing residues of EGF (N1 and S2 at the N-terminal end and E51, L52 and R53 at the C-terminal end) were built by using Discovery studio software package.

Figure 3.4 The sequences and components of the two studied system, EGFR•EGF and EGFR•EGF-CS-SWCNT-Drug that compose of total residue number of 665 and 727, respectively.

In case of EGFR•EGF-CS-SWCNT-Drug, the (18,0) SWCNT with 14 Å in diameter and 34 Å in length generated from Nanotube Modeler package [83] was chosen as a model of SWCNT where gemcitabine as anti-cancer drug (PDB codes 2NO0 [75]) was placed in the middle of the channel of the channel. The chitosan chain consisted of 60 units with 60% DD in a random sequence of NAG and GLS monomers was wrapped over pristine SWCNT outer surface (both end tips terminated with H). Then, EGF was covalently linked to the chitosan chain via a

peptide bond between R53 at the C terminal end of EGF and the first chitosan unit in the same manner as the section 3.4 [84] to obtain EGF-CS-SWCNT-Drug. After that, the EGF-CS-SWCNT-Drug was superimposed with EGF in EGFR•EGF to obtain EGFR•EGF-CS-SWCNT-Drug. The sequences of all components in the three systems are presented in Fig. 3.4. Parameters of the amino acids and SWCNT were taken from the AMBER ff03 force field where the atom types CA and C were chosen to represent the aromatic carbon atoms and the tertiary functionalized carbon atoms on the end tips, respectively, while the GLYCAM06 force field [82] was applied for chitosan. The parameters of gemcitabine were obtained as the same manner as section 3.2 and 3.3. [77,85]

(i) EGFR•EGF   **(ii) EGFR•EGF-CS-SWCNT-Drug**
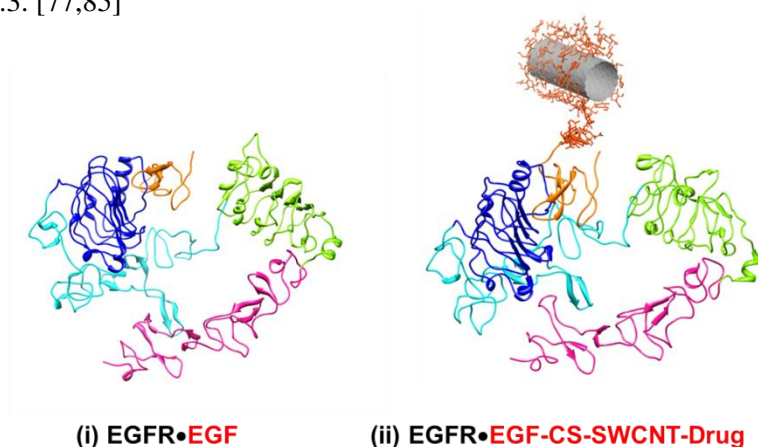
Figure 3.5 The 3D structures of the four systems studied: (i) EGFR•EGF, (ii) EGFR•EGF-SWCNT-Drug and (iii) EGFR•EGF-CS-SWCNT-Drug. The EGF and I-IV domains of EGFR are represented by orange, blue, cyan, green and pink, respectively.

MD simulations setup

The MD simulations were applied on three systems; (i) EGFR•EGF and (ii) EGFR•EGF-CS-SWCNT-Drug, as shown in a schematic view in Fig. 3.5. To set up the systems, the protonation state of the ionizable amino acids was assigned in the following manner: all Asp and Glu residues were considered to be negatively charged while all Arg and Lys residues were

treated as positively charged. Additionally, the disulfide bridges between two CYS residues were preserved by setting them as CYX. Afterward, all missing hydrogen atoms of proteins, SWCNT and gemcitabine were added with standard bond lengths and angles using the LEaP module of AMBER 10 [86]. Then, each system was solvated in the truncated cubic box of TIP3P water molecules. To neutralize the electrical charge of the system, sodium ions were randomly added in the EGFR•EGF and EGFR•EGF-CS-SWCNT-Drug complexes.

All simulations were carried out under the periodic boundary condition with the *NPT* ensemble using AMBER10. The particle mesh Ewald method [81] was used to handle the long-range electrostatic interactions, whilst the SHAKE algorithm [80] was employed to constrain all bonds involving hydrogen atoms. A time step of 2 fs and pressure of 1 atm with a cutoff of 12 Å for non-bonded interactions were applied. To reduce steric contacts prior to the simulation process, the hydrogen atoms were firstly minimized with all the heavy atoms fixed, followed by the optimization of the added water molecules and finally the minimization of the whole structure. All systems were heated to 298 K for 60 ps and then the MD simulations were performed for 50 ns. The MD trajectories were recorded every 500 steps and only the snapshots extracted after the system achieved the equilibrium were used for analysis.

CHAPTER IV

RESULTS AND DISCUSSION

4.1 The non-covalent interaction of nucleobases analogue anti-cancer drug with graphene
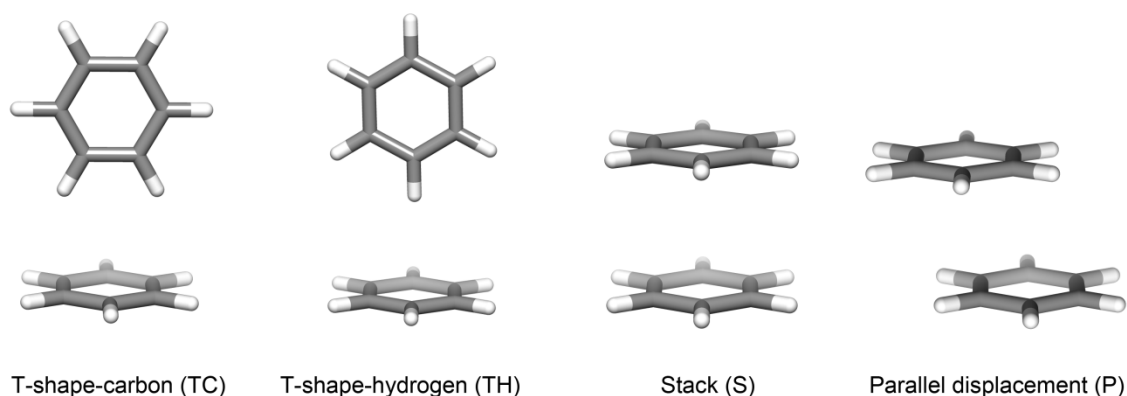
Figure 4.1 optimized geometries of benzene dimers

One of important interaction between aromatic compounds is the dispersion interaction. The dispersion interaction has been found to influence the orientation of DNA, proteins on carbon nanomaterials. [87] The simplest model that can be used to understand the dispersion interaction of aromatic compounds is benzene dimer. Hence, the binding energies of benzene dimer were investigated through the mimic models such as T-shape-carbon, T-shape-hydrogen, stack and parallel displacement conformation. These four dimers were optimized at several levels of accuracy, *i.e.* M06-2X, MP2, and CCSD(T) with cc-pVDZ level of basis sets in Gaussian 03. Optimized geometries obtained from M06-2X/cc-pVDZ were shown in Fig. 4.1. The obtained results from calculations with M06-2X/cc-pVDZ and MP2/cc-pVDZ reveal that the dimer in parallel displacement was the most stable complex when compared with 3 other conformations. However, the T-shape-hydrogen was the most stable form when calculated with CCSD(T)/cc-

pVDZ. This result is supported by the literature that MP2 overestimates the dispersion interaction in comparison to the higher accuracy method [88] such as CCSD(T), as shown in Table 4.1. The difference of binding energies of the four dimers at CCSD(T)/cc-pVDZ level were less than 1 kcal/mol suggesting that the energy surface of benzene dimer is very flat and, thus, many conformations of the dimer are possible.

Table 4.1 Binding energies (kcal/mol) of benzene dimers and complexes between coronene and benzene

Complex	Methods	TC	TH	S	P
dimer	M06-2X/cc-pVDZ	-2.98	-3.02	-1.70	-3.34
	MP2/cc-pVDZ	-4.11	-4.65	-3.51	-5.14
	CCSD(T)/cc-pVDZ //MP2/cc-pVDZ	-2.48	-2.88	-0.91	-2.00
C24^1/ benzene	ONIOM(MP2/cc-pVDZ : B3LYP/cc-pVDZ)	-2.93	-3.05	-4.06	-4.37
	ONIOM(CCSD(T)/ cc-pVDZ : B3LYP/cc-pVDZ)	-2.14	-2.21	-1.50	-1.96
C24^2/ benzene	ONIOM(MP2/cc-pVDZ : B3LYP/cc-pVDZ)	-4.07	-4.04	-6.26	-8.07
	ONIOM(CCSD(T)/ cc-pVDZ : B3LYP/cc-pVDZ)	-2.94	-3.88	-3.02	-3.65
C24/ benzene	M06-2X/cc-pVDZ	-3.11	-3.08	-7.71	-8.64

Remark: C24^1 = coronene with high layer of central 6 carbon atoms in ONIOM method. and C24^2 = coronene with high layer of 10 carbon atoms in ONIOM method as shown structure in Fig. 4.2.

C24^1 : C24 with high level
in 6 carbon atoms region

C24^2 : C24 with high level
in 10 carbon atoms region
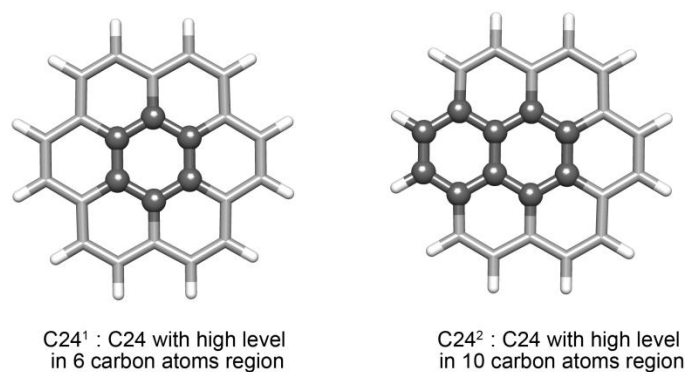
Figure 4.2 The models of C24 for ONIOM calculation, (left) the 6 carbon atoms and (right) 10 carbon atoms at high layer labeled in black while atoms in low layer were in grey.

C24^1/Benzene-TC   C24^1/Benzene-TH   C24^1/Benzene-S   C24^1/Benzene-P

C24^2/Benzene-TC   C24^2/Benzene-TH   C24^2/Benzene-S   C24^2/Benzene-P
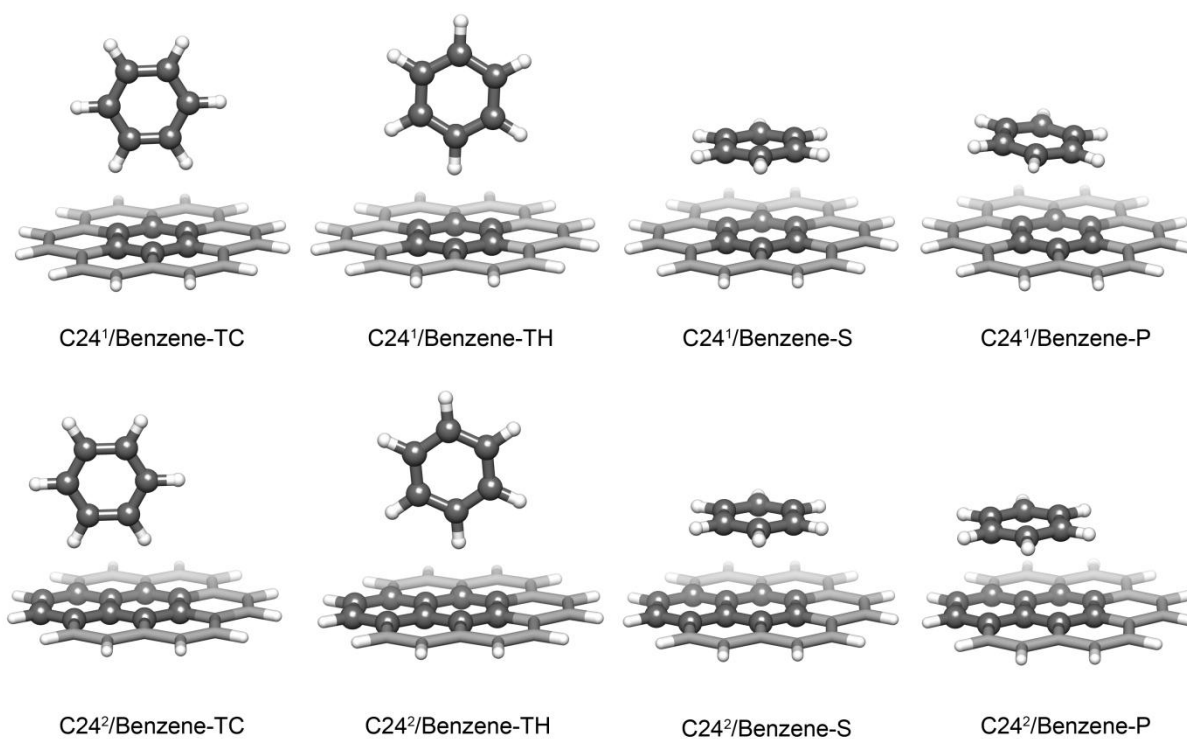
Figure 4.3 Optimized geometries of coronene/benzene complexes at MP2/cc-pVDZ : B3LYP/cc-pVDZ.

To give more details about the dispersion of aromatic ring, the binding of benzene with coronene $C_{24}H_{12}$ were investigated by four conformations in the same manner as the benzene dimers. To reduce computational time, the ONIOM (our own n-layered integrated molecular orbital and molecular mechanics) method [89] developed by Morokuma and co-worker [89,90], was applied in which the MP2/cc-pVDZ or the CCSD(T)//cc-pVDZ was used in high layer while B3LYP/cc-pVDZ were taken for low layer. Two models of ONIOM were applied for calculating the binding of benzene with coronene (C24). In the first model, the center 6 carbon atoms of C24 and benzene were selected as the high layer while for another model 10 carbon atoms of C24 were chosen as shown in Fig. 4.2. The results of these calculations are presented in Table. 4.1 and Fig. 4.3. It can be noticed that when the size of the high layer is increased, the binding energy

also increased. For example, the binding of benzene in parallel displacement was increased from -4.37 to -8.07 kcal/mol and -1.96 to -3.65 kcal/mol at MP2/cc-pVDZ: B3LYP/cc-pVDZ and CCSD(T)//cc-PVDZ: B3LYP/cc-pVDZ, respectively. The binding of benzene complex with C24 was in the same trend with that of benzene dimer *e.g.* the T-shape dimers were the most stable forms in the calculation with CCSD(T) but were less stable than the parallel forms when calculated with MP2. The four complexes were fully optimized at M06-2XM06-2X/cc-pVDZ and the obtained results are in agreement with MP2/cc-pVDZ: B3LYP/cc-pVDZ as shown the results in Table 4.1. All of these results suggest that both MP2 and M06-2x overestimate the dispersion of benzene adsorption when compared to CCSD(T) level. In another hand, without proper description of dispersion energy the parallel form is preferred. Thus, the accuracy of the method should be of concerned.

To understand the binding of small biomolecule with graphene, the interactions between nucleobases and analogue anti-cancer drugs with graphene were investigated. The details of binding interactions were divided into i) the adsorption of nucleobases and ii) the adsorption of analogue anti-cancer drugs.

The adsorption of nucleobases

Table 4.2 The distances (in Å) between nucleobase and graphene

	C24				C54				C96	
	M06-2X/ 6-31G(d)	M06-2X/ cc-pVDZ	M06-2X/ cc-pVTZ	B97-D/ TZV(d,p)	M06-2X/ 6-31G(d)	M06-2X/ cc-pVDZ	M06-2X/ cc-pVTZ	B97-D/ TZV(d,p)	M06-2X/ 6-31G(d)	B97-D/ TZV(d,p)
A	3.29	3.31	3.32	3.26	3.29	3.29	3.30	3.11	3.29	3.03
C	3.28	3.28	3.30	3.19	3.27	3.27	3.29	3.04	3.27	2.97
G	3.27	3.28	3.30	3.20	3.27	3.27	3.29	3.05	3.27	3.01
T	3.26	3.26	3.29	3.23	3.26	3.26	3.28	3.10	3.25	3.01
U	3.25	3.25	3.28	3.22	3.25	3.26	3.27	3.09	3.25	3.00

For the adsorption of nucleobases, the A, C, G, T and U in complex with three graphene sheets (C24, C54 and C96) were fully optimized by using M06-2X with 6-31G6-31G(d), cc-pVDZ and cc-pVTZ basis sets. All nucleobases are located at the center of graphene flake in the partial parallel displacement as illustrated by the optimized geometries of nucleobase with the three graphene sheets in Figs. 4.4-4.6. The average distances between the nucleobase heavy atoms and graphene surfaces have been reported in Table 4.2. The range of the obtained distances is in agreement with the thickness of monolayer of guanine and adenine on graphite of 3 Å by atomic force microscopy (AFM) [91]. Compared with the DFT-D study at B97-D/TZV(d,p) from Antony and Grimme [9], the observed distances of all nucleobase are a little bit longer *e.g.* the distance of A to C96 is 3.29 Å at M06-2X/6-31G6-31G(d) while those of B97-D/TZV(d,p) is 3.03 Å. In addition, the result suggests that the distances between nucleobases and graphene depend on the level of basis set. When the level of basis set increases, *i.e.* from cc-pVDZ to cc-pVTZ, longer distances between nucleobases and graphene are observed. For example, the distance of C to C54 increases from 3.27 to 3.29 Å when the basis set is altered from cc-pVDZ to cc-pVTZ. Moreover, the size of graphene is found to influence the binding of nucleobase. When the size of graphene model is increased, the nucleobases locate closer to that graphene surfaces as shown by shorten of the distances in C54 and C96 complexes compared with C24, as seen in Table. 4.2.

C24/G   C24/A

C24/T   C24/C   C24/U
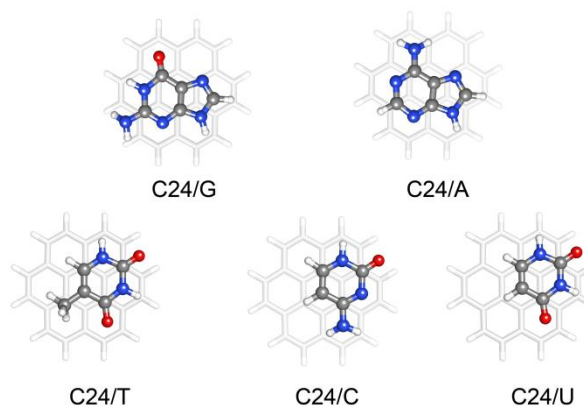
Figure 4.4 Optimized geometries of complexes between nucleobase and graphene (C24) in order of their binding energies (G > T > C > A > U).
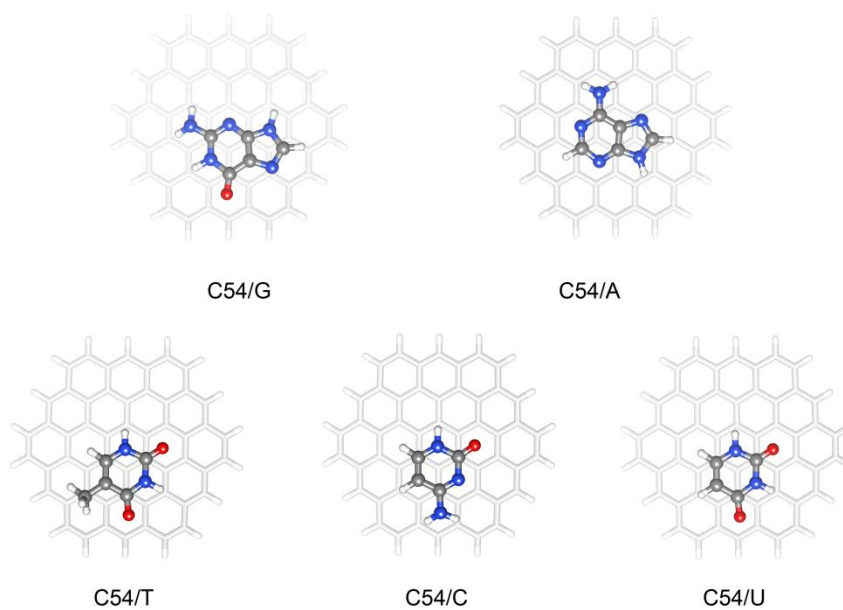
Figure 4.5 Optimized geometries of complexes between nucleobase and graphene (C54) in order of their binding energies (G > A > T > C > U).
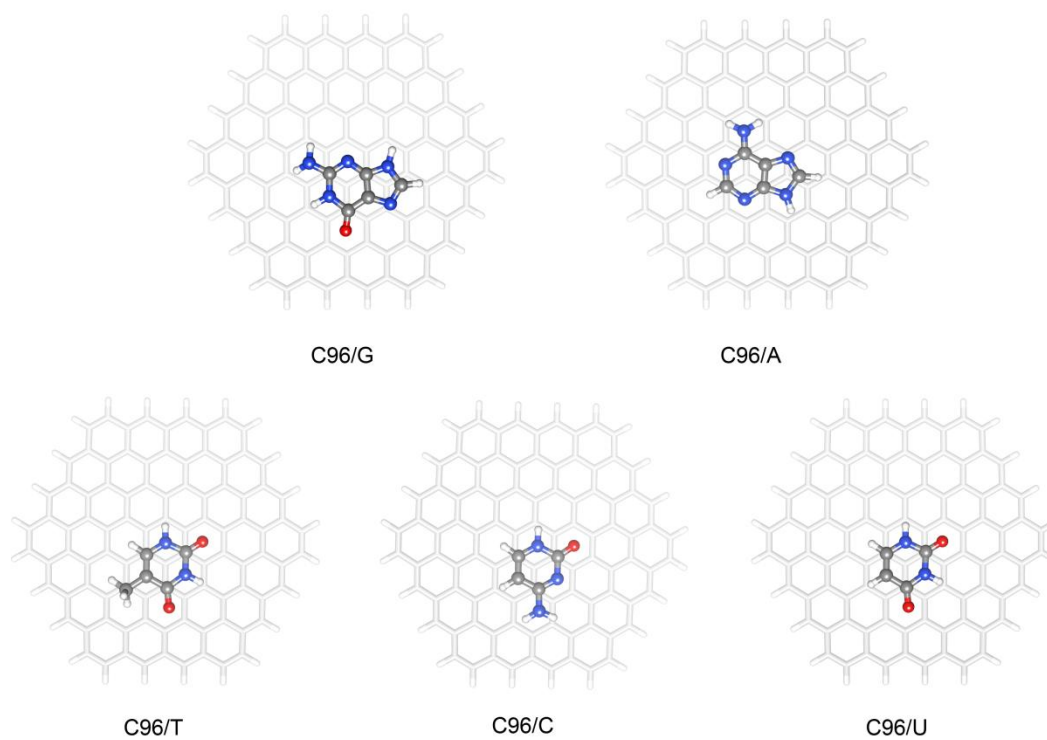
Figure 4.6 Optimized geometries of complexes between nucleobase and graphene (C96) in order of their binding energies (G > A > T > C > U).

In term of binding energy, the obtained interaction energies reveal that the size of graphene influences the binding of the bases, as presented in Table. 4.3. To eliminate basis set superimposition error (BSSE), the counterpoise correction method was applied and the BSSE corrected interactions were presented in parentheses in Table 4.3. As expected, the differences between calculated binding energies with and without BSSE correction are reduced when the level of basis set is increased. For example, the binding energies of A to C24 without BSSE correction at M06-2X with 6-31G6-31G(d), cc-pVDZ and cc-pVTZ are -14.57, -15.25 and -12.87 kcal/mol while those with BSSE correction are -9.60, -10.88 and -11.17 kcal/mol, respectively. These data suggest that the accuracy from calculation by M06-2X method at 6-31G6-31G(d) and cc-pVDZ are not proper enough when compared with the calculation at cc-PVTZ because their BSSE correction energies are smaller than the cc-pVTZ result. In addition, the BSSE corrected binding energies of purine base (A and G) raised up about 2 kcal/mol when the size of graphene increased from C24 to C54 and slightly increases about 0.1 kcal/mol from C54 to C96. The purine base binding energies obtained using C54 and C96 are in good agreement with results at M06-2X/TZV(2d,2p). [8] However, when compared with B97D/TZV(2d,2p) the binding energies obtained in this   work are smaller for all graphene sizes. For example, the binding energies of A at B97D/TZV(2d,2p) were -14.20, -19.30 and -20.20 kcal/mol for C24/A, C54/A and C96/A, respectively, while at M06-2X/6-31G6-31G(d) were -14.57, -16.24 and -16.19 kcal/mol.

In C24 complex, graphene sheet is too small and the edge effect may perturb the binding, (see Fig. 4.4). The interaction energy was in the sequence of G > T > C > A > U where the binding complex of A was the less stable than T and C although A contains larger aromatic conjugate than the two pyrimidine base. When the graphene size is large enough *i.e.* C54 and C96 (see respectively Figs. 4.5-4.6), this edge effect can be eliminated and the binding order change to G > A > T > C > U which is the same order as obtained by both experimental studies [3,92]

and previous theoretical studies [9,93,94]. Therefore, the size of graphene sheet that suitable for the adsorption of nucleobase should be larger than C24 or at least around 54 carbon atoms [9].

Taken altogether, the M06-2X method can give reasonable results for the non-covalent interaction of nucleobase and graphene and is in good agreement with other DFT-D studies. Thus, the M06-2X were applied to the study of non-covalent interaction of nucleobase analogue anti-cancer drugs with graphene. It is worthwhile to note that only C54 and C96 size of graphene sheet were selected for that investigation to reduce the edge effect as discussed above.

Table 4.3 Binding energies (kcal/mol) of nucleobases with different size of graphene sheets. The values in parentheses are the binding energies with BSSE correction.

	method	A		C		G		T		U	
C24	M06-2X/6-31G(d)	-14.57	(-9.60)	-15.12	(-10.57)	-18.55	(-13.35)	-15.61	(-11.07)	-13.52	(-9.35)
	M06-2X/cc-pVDZ	-15.25	(-10.88)	-15.64	(-11.56)	-19.24	(-14.40)	-16.07	(-12.06)	-13.98	(-10.25)
	M06-2X/cc-pVTZ	-12.87	(-11.17)	-13.64	(-12.06)	-16.72	(-14.89)	-14.09	(-12.71)	-12.23	(-10.89)
	M06-2X/TZV(2d,2p)[a]	-11.70		-13.30		-15.80		-12.60		-10.90	
	DFT-D/TZV(2d,2p)[a]	-13.80		-13.30		-16.80		-13.50		-11.50	
	B97D/TZV(2d,2p)[b]	-14.20		-13.70		-18.30		-15.40		-13.20	
C54	M06-2X/6-31G(d)	-16.24	(-11.34)	-15.04	(-10.24)	-19.76	(-14.12)	-15.73	(-10.97)	-13.64	(-9.23)
	M06-2X/cc-pVDZ	-17.40	(-12.81)	-15.92	(-11.40)	-21.09	(-15.56)	-16.47	(-12.08)	-14.47	(-10.32)
	M06-2X/cc-pVTZ	-14.92	(-13.06)	-14.05	(-12.24)	-18.36	(-16.19)	-14.41	(-12.81)	-12.59	(-11.06)
	M06-2X/TZV(2d,2p)[a]	-13.80		-13.60		-17.30		-13.70		-12.10	
	DFT-D/TZV(2d,2p)[a]	-18.40		-16.00		-21.80		-16.90		-14.60	
	B97D/TZV(2d,2p)[b]	-19.30		-17.80		-23.30		-18.00		-15.40	
C96	M06-2X/6-31G(d)	-16.19	(-11.35)	-15.13	(-10.39)	-19.84	(-14.22)	-15.63	(-10.90)	-13.48	(-9.06)
	M06-2X/TZV(2d,2p)[a]	-13.80		-13.60		-17.70		-14.00		-12.30	
	DFT-D/TZV(2d,2p)[a]	-19.20		-17.00		-23.00		-17.90		-14.80	
	B97D/TZV(2d,2p)[b]	-20.20		-18.50		-24.20		-19.00		-16.30	

[a] from the study of Ramraj et.al. [8] and [b] from the study of Antoney and Grimme [9]

The adsorption of nucleobase analogue anti-cancer drugs

To investigate the adsorption of four nucleobase analogue anti-cancer drugs, F, GC, MP and TG, the distances between heavy atoms of drugs and carbon atoms of graphene were calculated and presented in Table. 4.4. At the same time the optimized geometries of the four anti-cancer drugs with C54 and C96 were shown in Fig. 4.7 and 4.8, respectively. Since the size of C54 and C96 are large enough for the nucleobase analogue adsorption, observed distances between drugs and C54 and C96 are quite similar. For example, the distance of F to C54 surface is 3.22 Å while that of F to C96 surface is 3.21 Å at M06-2X/6-31G(d). The closest distance to C54 at the highest level of basis set, cc-pVTZ, was the adsorption of smallest drug, F, around 3.22 Å while the longest distance was the adsorption of GC due to the steric hindrance of its substitute group (3.96 Å). The optimized structures of C54/GC and C96/GC reveal that the drug parallels to graphene surface and points the ribose group out of the surface as shown in Figs. 4.7 and 4.8. This result supports the MD simulations of gemcitabine encapsulation inside SWCNT from Arsawang, U. and coworker [77] who indicated the close contact of cytosine ring from gemcitabine instead of its steric ribose group. Moreover, the adsorption of the purine derivatives (MP and TA) located close to the C54 surface at 3.34 and 3.33Å, respectively, at cc-pVTZ which were slightly longer around 0.04 Å compared with the standard nucleobase A and G.

Table 4.4 The distances (in Å) between anti-cancer drug and graphene with M06-2X

	C54			C96
	6-31G(d)	cc-pVDZ	cc-pVTZ	6-31G(d)
F	3.22	3.22	3.22	3.21
GC	3.94	3.91	3.92	3.94
MP	3.32	3.33	3.34	3.30
TG	3.32	3.32	3.33	3.31
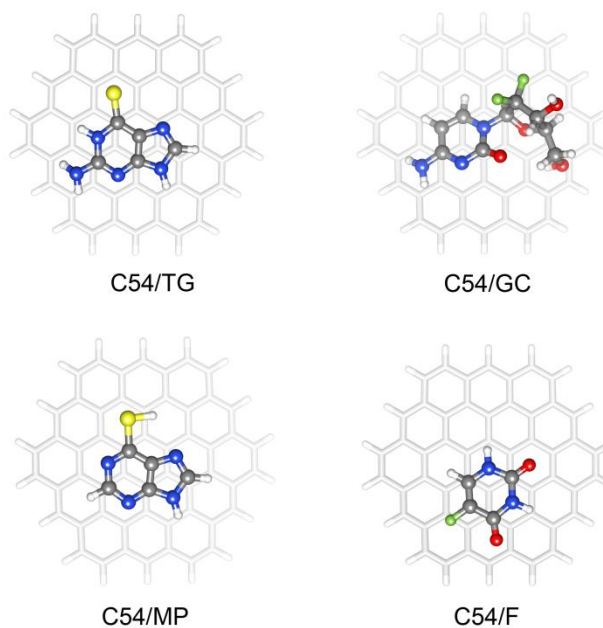
Figure 4.7 Optimized geometries of anti-cancer drug and graphene (C54) complexes in order of the binding energies (TG > GC > MP > F).
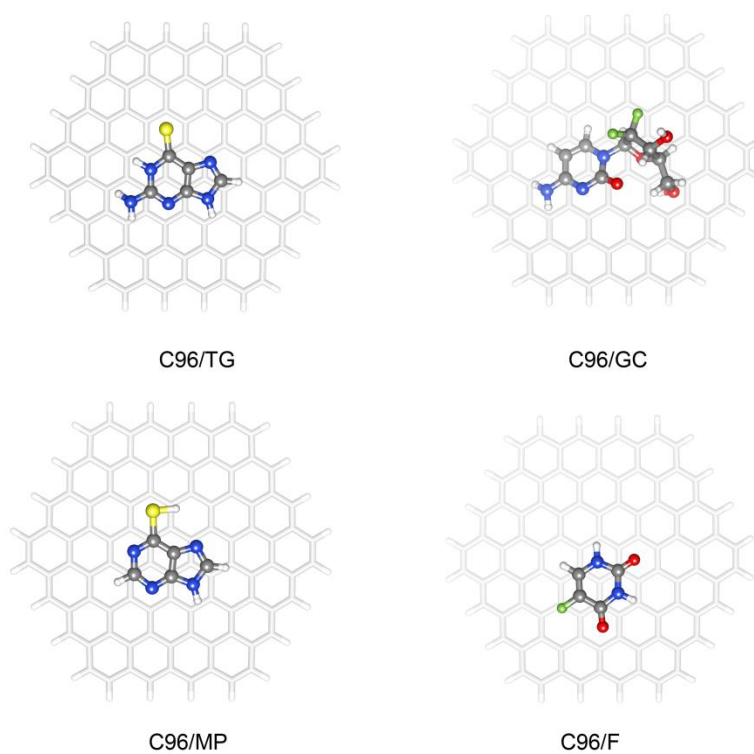
Figure 4.8 Optimized geometries of anti-cancer drug and graphene (C96) complexes in order of the binding energies (TG > GC > MP > F).

Table 4.5. Binding energies (kcal/mol) of analogue anti-cancer drug of nucleobases with different aromatic compounds represented for graphene sheet. The values in parentheses are the binding energy with BSSE correction.

	method	MP	GC	TG	F
	M06-2X/6-31G(d)	-15.51 (-11.32)	-18.44 (-12.19)	-20.36 (-15.29)	-14.80 (-10.23)
C54	M06-2X/cc-pVDZ	-16.97 (-13.11)	-19.56 (-13.18)	-20.02 (-16.96)	-15.53 (-11.19)
	M06-2X/cc-pVTZ	-14.54 (-12.98)	-16.42 (-13.71)	-19.06 (-17.14)	-13.42 (-11.44)
C96	M06-2X/6-31G(d)	-15.34 (-11.21)	-17.94 (-11.65)	-20.02 (-16.96)	-14.36 (-9.34)

From Table. 4.5, the sequence of the binding at all levels of basis sets and all graphene sizes are in the same sequence, TG > GC > MP > F, where their BSSE correction binding energies at cc-pVTZ basis set are -17.14, -13.71, -12.98 and -11.44 kcal/mol, respectively. As expected, the smallest anti-cancer drug, F, has smallest binding energy when compared to drugs with larger aromatic group, *i.e.,* purine base analogues (MP and TG). Note that the binding energy of F and standard nucleobases, T and U, is in the sequence of T > F > U at all levels of calculation. This implies that the strength of substitute group in pyrimidine based on the binding with graphene is in the order of CH_3 > F > H. Moreover, the large substitute group of GC was found to destabilize in the adsorption with graphene as shown by the higher binding energy around 1 kcal/mol compared to its standard nucleobase C.

In case of the TG, the adsorption of purine with the thione group gives the highest interaction energy (-17.14 kcal/mol at cc-pVTZ basis set with BSSE correction) which is higher than the standard base G around 1 kcal/mol. The result implies that the thioketo functional group binds with graphene stronger than the ketone group. For MP, the binding energy calculation with BSSE correction is quite similar to its standard nucleobase, A, (differ by less than 1 kcal/mol)

suggesting that the effect of thiol group is quite similar with amine group in the binding interaction with graphene. Moreover, the tautomer of MP and TG were also investigated in the thiol and thione conformation and present the optimized geometries in Fig. 4.14. The thione tautomer of both MP and TG form a more stable complex with graphene than their thiol conformations at all levels of theory, as shown details in Table. 4.6. From these results, it can be noted that larger aromatic conjugated of the drug can promotes its binding stability with graphene.

Table 4.6. Binding energies (kcal/mol) of tautomer (in thiol and thione conformations) of MP and TG. The values in parentheses are the binding energies with BSSE correction.

	method	MP (thiol)		MP (thione)		TG (thiol)		TG (thione)	
	M06-2X/6-31G(d)	-15.51	(-11.32)	-16.79	(-12.60)	-18.34	(-13.21)	-20.36	(-15.29)
C54	M06-2X/cc-pVDZ	-16.97	(-13.11)	-18.29	(-14.29)	-20.09	(-15.10)	-20.02	(-16.96)
	M06-2X/cc-pVTZ	-14.54	(-12.98)	-16.03	(-14.45)	-17.09	(-14.87)	-19.06	(-17.14)

C54/Thione-TG   C54/Thiol-TG

C54/Thione-MP   C54/Thiol-MP
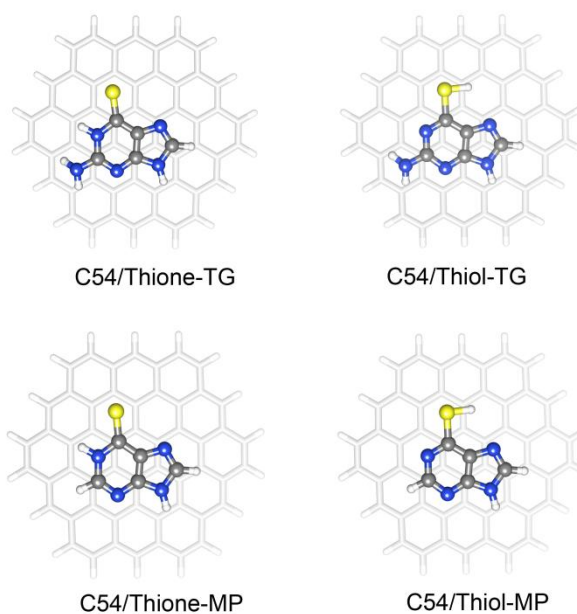
Figure 4.9 Optimized geometries of MP and TG tautomers in thione and thiol conformations.

4.2 Investigation of the orientation of doxorubicin over graphene
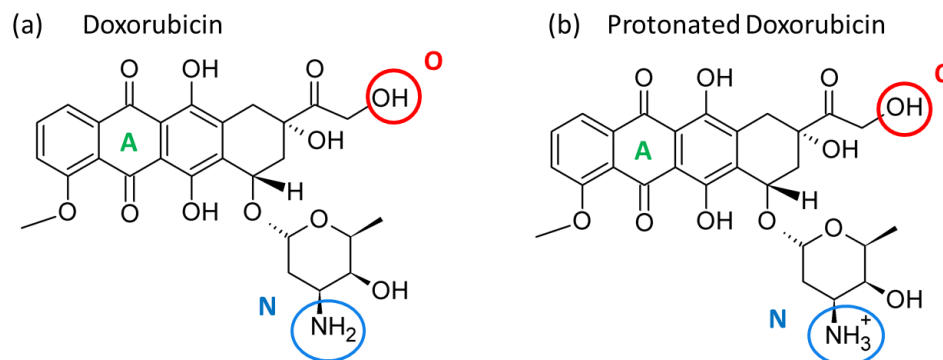
Figure 4.10 The structures of neutral and positively charged doxorubicins with labels of aromatic ring system (A), hydroxyl group (O) and amine group (N).

From the geometry optimization of 500 complexes different drug orientation over graphene, the distance from graphene to the aromatic ring system (A), the hydroxyl group (O) and the amine group (N), as labelled in Fig. 4.10(a), of all 500 complexes denoted as d(Graphene-A), d(Graphene-O) and d(Graphene-N), respectively, are calculated. The plots of d(Graphene-A) versus d(Graphene-N) as well as d(Graphene-A) versus d(Graphene-O), Figs. 4.11(a-b), respectively, show that the interaction energies of all 500 complexes are in the range of -10 to -70 kcal/mol. In addition, complexes with distance d(Graphene-A) around 3.5 Å are more stable than other conformation suggested by their interaction energies of -70 to -60 kcal/mol. To evaluate the orientation of the doxorubicin, the four complexes are selected and labelled as 1, 2, 3 and 4 as illustrated in Fig. 4.11. It is clearly seen that complexes with the drug in parallel to graphene surface (complex 1and 2) are more stable than the others. Therefore, this implies that the π-π interaction is more important than electrostatic effect from heteroatoms in the binding between neutral doxorubicin and graphene.

To confirm this hypothesis, the interaction energies are decomposed into electrostatic and vdW as presented in the z axis of Fig.4.12. It can be recognized from the plots that the vdW interaction energies, INT(V) are in the range of -10 to -70 kcal/mol which are larger than interaction energies from electronic term, INT(E), that are in the range of -2 to 1.5 kcal/mol. Hence, all data indicate that the binding between aromatic anti-cancer drug mainly comes from dispersion interaction as shown in the high amount of vdW energies.
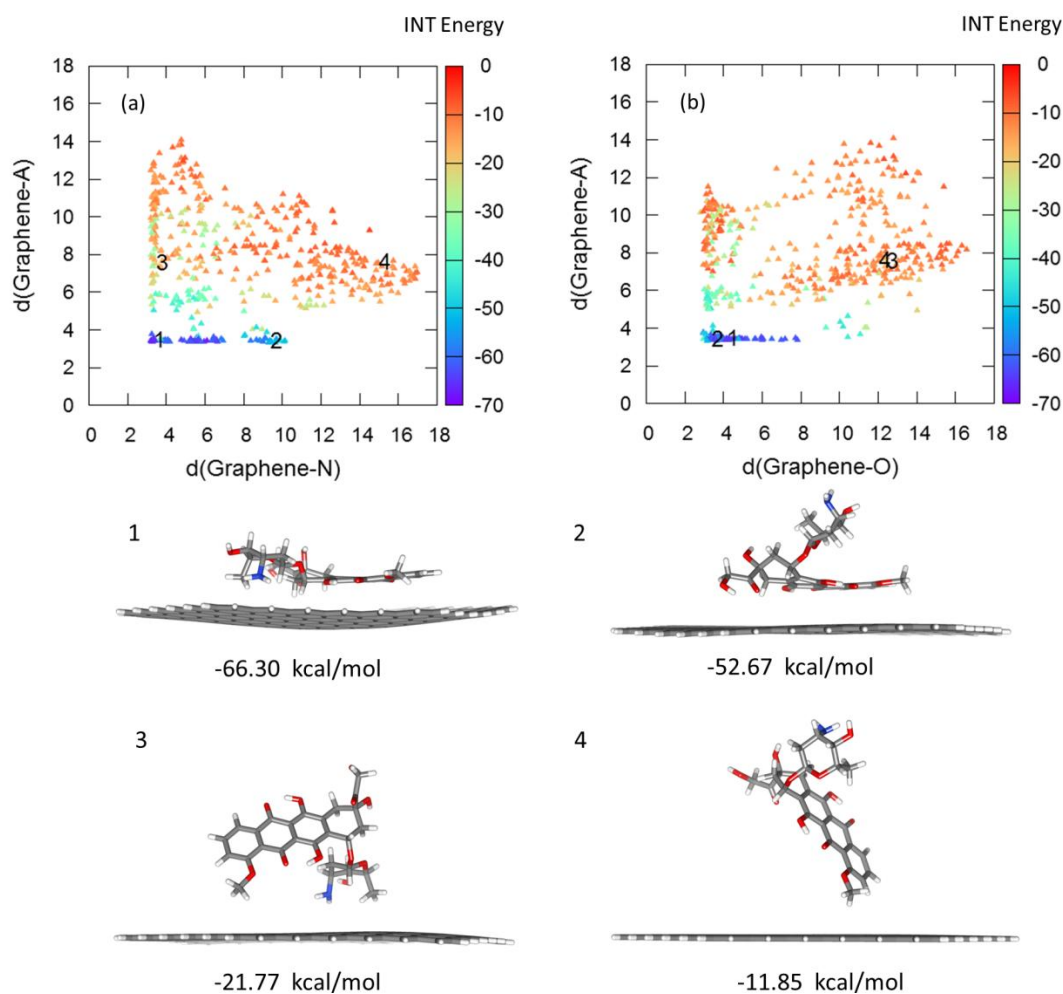
Figure 4.11 The 2D total interaction (INT) energy plots of (a) d(Graphene-A) versus d(Graphene-N) and (b) d(Graphene-A) versus d(Graphene-O) with the representative complexes labelled as 1, 2, 3 and 4.
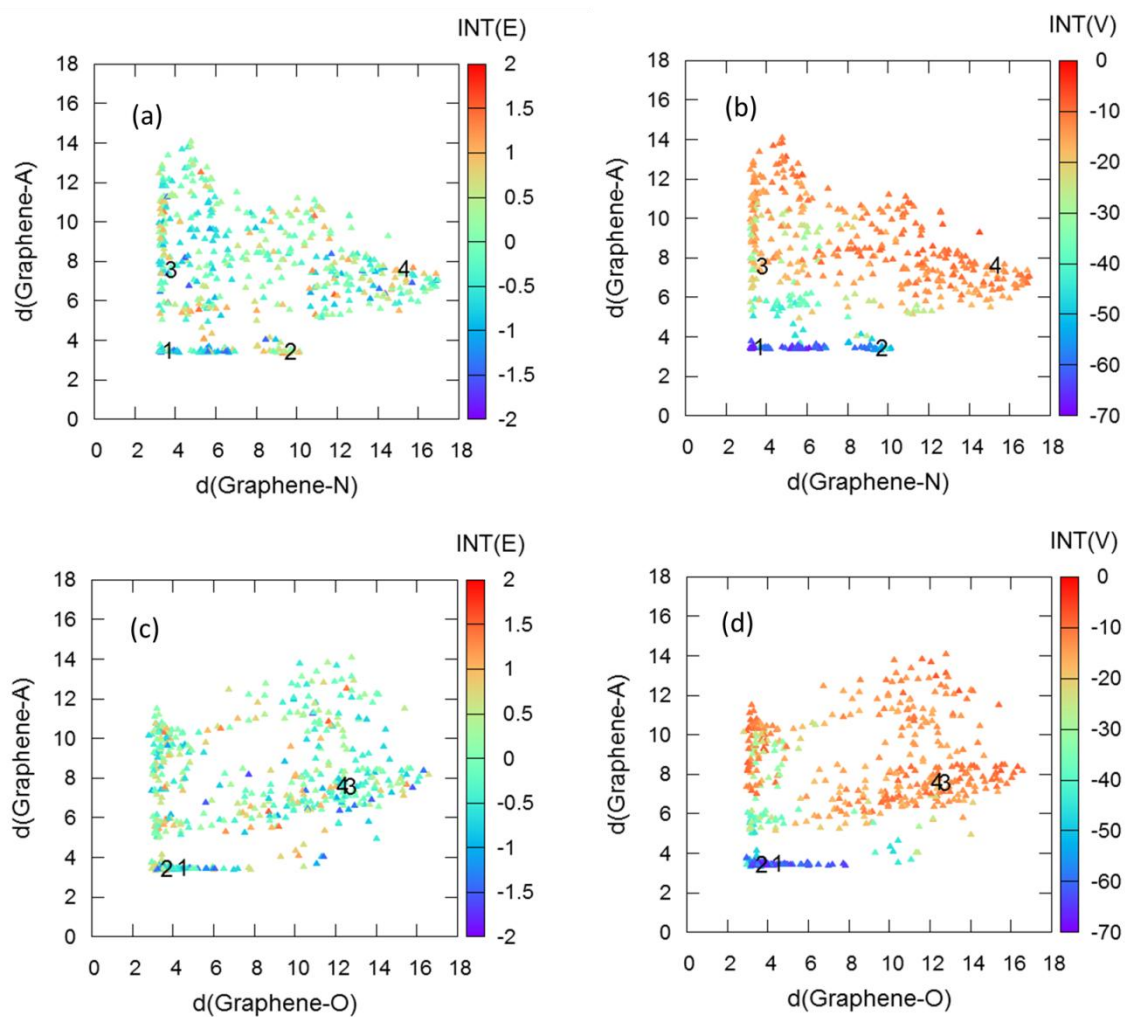
Figure 4.12 (a)-(b) Electronic, INT(E), and (c)-(d), van der Waals (vdW) energies in kcal/mol from the binding of doxorubicin and graphene in relation with d(Graphene-A) and d(Graphene-N) and d(Graphene-A) and d(Graphene-N), respectively.

Because the approximated pKa of doxorubicin amino group is 7.6 [95], this amino group can be protonated in pure water condition as presented the positively charged structure in Fig. 4.10(b). To investigate the adsorption of the protonated doxorubicin over graphene, 500 complexes of protonated doxorubicins were generated and optimized by using DFTB-D in the same manner with the adsorption of the neutral form. The d(Graphene-A), d(Graphene-O) and d(Graphene-N) of each complex are calculated and plotted in Fig. 4.13. The pattern of the d(Graphene-N) versus the d(Graphene-A) is quite similar with the results from neutral doxorubicin adsorption in which the drug lined it aromatic conjugation parallel to graphene surface is more stable than the other positions as shown in Fig. 4.13(a). Moreover, the complex with positively charged amino group located close to graphene surface and the aromatic ring parallel to the surface is more stable than other conformation. For example, both of the complex 1 and 2 in Fig. 4.13 are parallel with graphene surface but the complex 1 having protonated amino group closer to graphene surface is more stable indicating the effect of cation-π interaction from protonated amino group. When the drug did not line parallel to graphene surface the binding energy is not favour even the protonated amino group is closer to the graphene like the complex 3 in Fig. 4.13. Because of the influence from cation-π interaction between the protonated group and graphene, the lowest interaction energy of protonated doxorubicin (-81.43 kcal/mol) is lower than that of the neutral drug (-66.30 kcal/mol). However, the effect from cation-π interaction is not strong as the π-π interaction since the binding energy decomposition in Fig. 4.14 reveals that the INT(V) is lower than INT(E). Additionally, the effect of doxorubicin hydroxyl group has not strongly impacted on the binding of the drug with graphene suggesting from non-pattern of INT (E) in Fig. 4.14(c) compared to total INT in Fig.4.13(b). The obtained data of the binding of both neutral and positively charged doxorubicin with graphene disclose that binding of drug or guest

molecule with graphene do not only depend on the π-π interaction between aromatic conjugated of the two molecules but the charge of guest molecule also influence the stability of the complex.
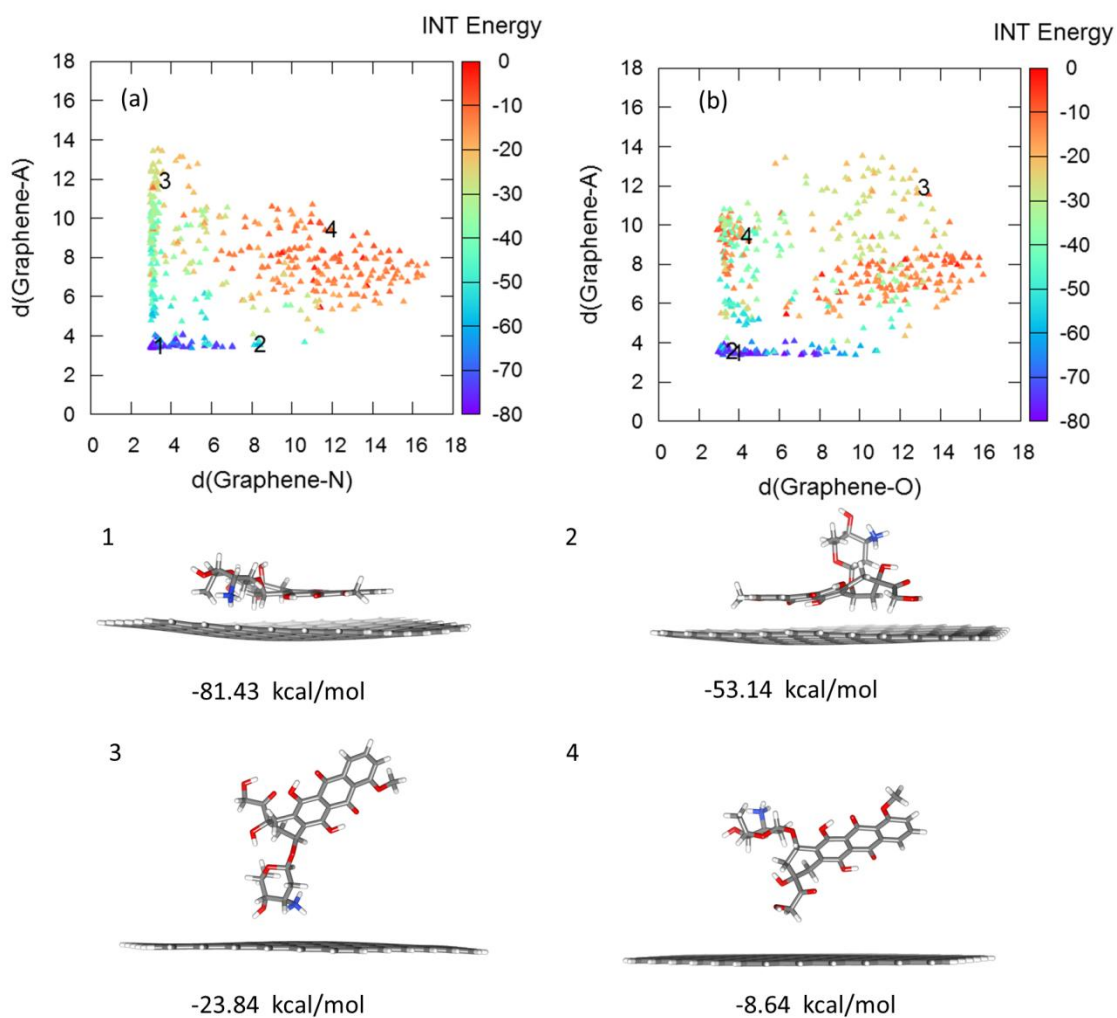
Figure 4.13 The 2D interaction (INT) energy plot of (a) distance from graphene to A and N, (b) distance from graphene to A and O with the representative complexes labelled as 1, 2, 3 and 4 in the complex between positively charged doxorubicin and graphene.
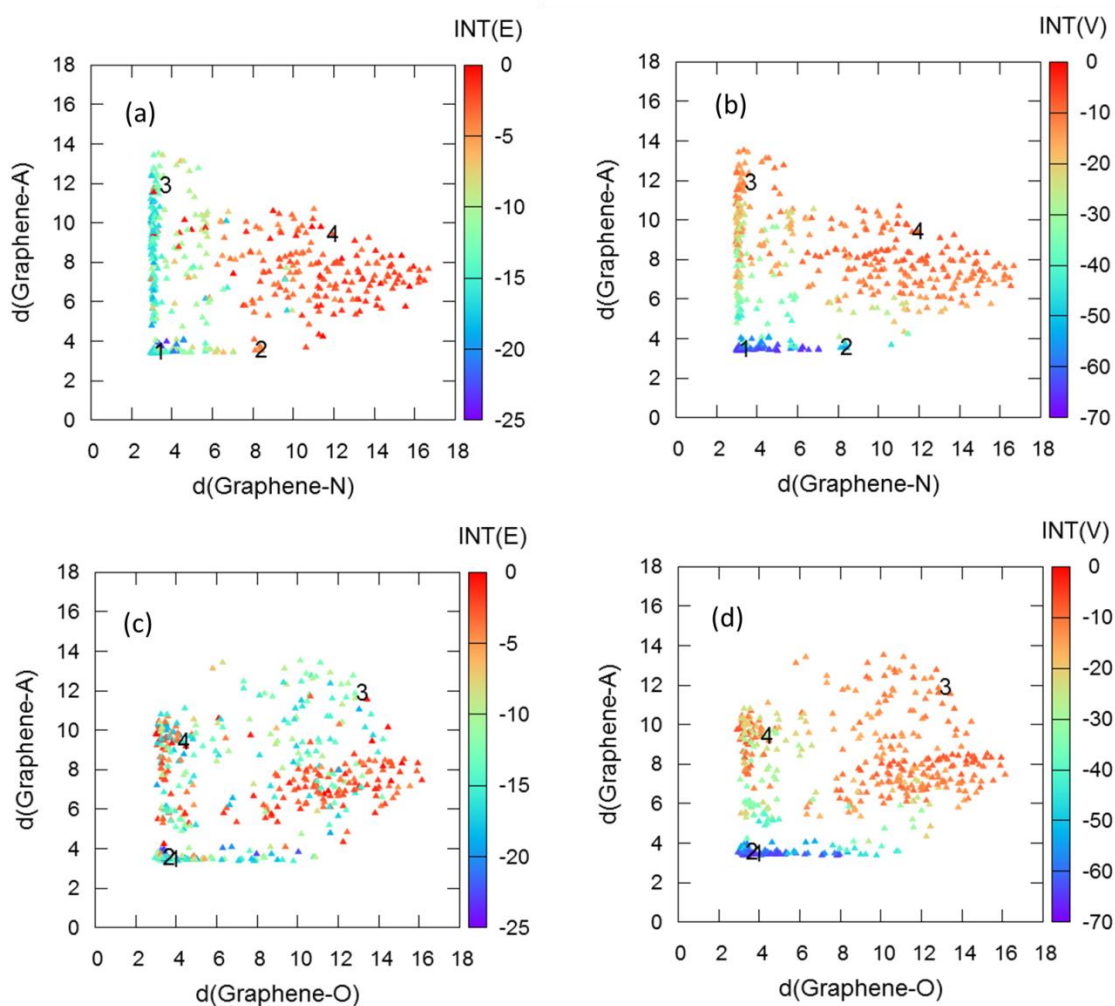
Figure 4.14 (a)-(b) Electronic, INT(E), and (c)-(d), van der Waals (vdW) energies in kcal/mol from the binding of positively charged doxorubicin and graphene in relation with d(Graphene-A) and d(Graphene-N) and d(Graphene-A) and d(Graphene-N), respectively.

4.3 Gemcitabine anti-cancer drug loading capacity of carbon nanotube

The molecular properties of gemcitabines varied from one to six molecules inside SWCNT cavity were investigated by classical MD simulation for 10 ns.
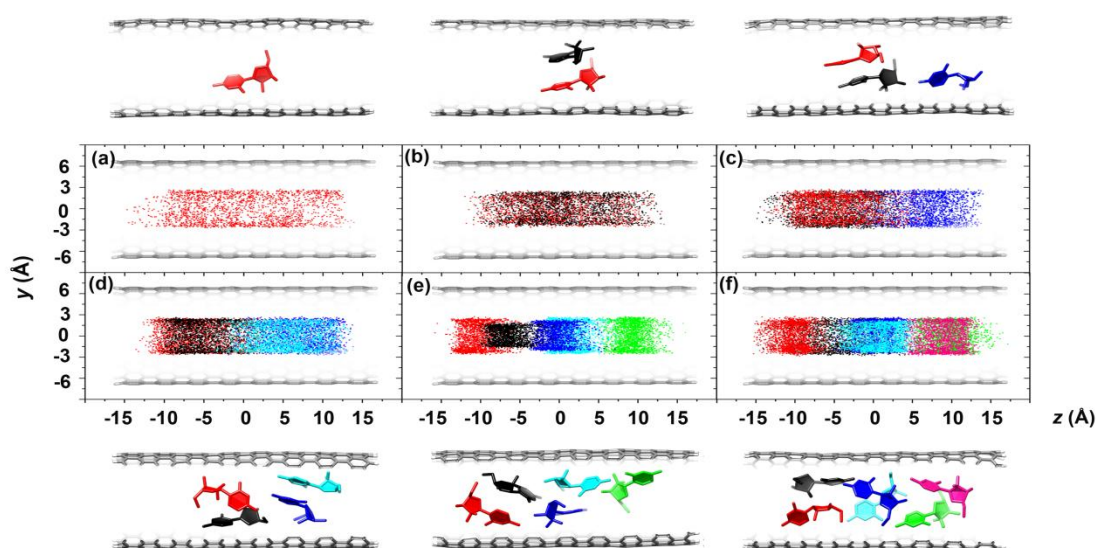
Figure 4.15 Displacement of the center of drug gravity,$\rho(Cg)$, projected to the YZ plane in the six studied systems: (a) 1-GEMZAR, (b) 2-GEMZAR, (c) 3-GEMZAR, (d) 4-GEMZAR, (e) 5-GEMZAR and (f) 6-GEMZAR. The representative structures taken from the last snapshot of each system are also shown schematically.

After MD simulation of the six systems with different drug amounts, all the drug molecules still encapsulated inside the SWCNT cavity due to the partial π-π interactions between gemcitabine molecules and the SWCNT [77]. The density plots of drug center gravity, $\rho(Cg)$, projected to the YZ plane are shown in Figs. 4.15(a-f) for i-GEMZAR systems where i = 1-6, where the gemcitabine molecules 1-6 (drug#1, drug#2, drug#3, drug#4, drug#5 and drug#6) are denoted by red, black, blue, cyan, green and pink, respectively. Among the six systems, only the drug positions in the 1-GEMZAR and 2-GEMZAR systems located throughout the tube cylinder as can be seen by the dispersion of red and black dots in Figs. 4.15a and 4.15b. For the systems with high loaded gemcitabine (3-, 4-, 5- and 6- GEMZAR), the drug molecules were found in a

limited space, see Figs. 4.15(c-f). These density plots suggest that the gemcitabine molecules favored to locate close to each other. Therefore, interactions among drug molecules were important in the drug displacement inside the SWCNT cavity.

Interaction between gemcitabine and SWCNT

Since both gemcitabine and SWCNT transporter contain aromatic rings, then, π-π stacking interactions are expected to be established between the cytosine ring of gemcitabine and the SWCNT inner wall surface. To understand the characteristics of this interaction in each system, the distribution of distances measured from the tube surface to the C^6 and N^1 atoms of all drugs, $d(C^6)$ and $d(N^1)$, were calculated and are plotted in Fig. 4.16. The narrow distributions of $d(C^6)$ and $d(N^1)$, with the most probable distances at 3.6 and 4.5 Å, respectively, together with a minimum and maximum variation of only ~0.5 Å, were found in the 1-GEMZAR (Fig. 4.16a). Without the effect from other drugs, the $d(C^6)$ and $d(N^1)$ values obtained in the 1-GEMZAR system were considered as a reference location for discussion with the other systems (1- to 6-GEMZAR). The most probable angle, Θ, between the vector lining from C^6- to N^1-cysteine atoms of gemcitabine and the SWCNT vector from the parallel orientation to the inner surface of the SWCNT was 19° (see schematic in Fig. 4.16 for definition). This data implied that gemcitabine arranges its cytosine ring in line with a parallel-displaced conformation to the SWCNT surface, while the five-membered ring was pointed to the tube center to avoid steric effects. The $d(C^6)$ value in 1-GEMZAR was in good agreement with the related distance between the cytosine and benzene rings of 3.5 Å obtained from the MD simulations using the MP2 level of theory (dashed line in Fig. 4.16) [96]. In the case of the systems containing higher gemcitabine loadings, the most frequent finding for the location of $d(C^6)$ was within the same range, ~3.6-3.7 Å, but with a broader peak starting at the equivalent distance of 3.1 Å but ending at longer distance by > 1.0 Å. However, a different situation was observed for the $d(N^1)$ distribution with a rather broad and

more than one peak falling in the range of ~3.9-6.2 Å for the 2-, 3- and 5- GEMZAR systems and ~3.3-6.0 Å for the 4- and 6- GEMZAR systems.
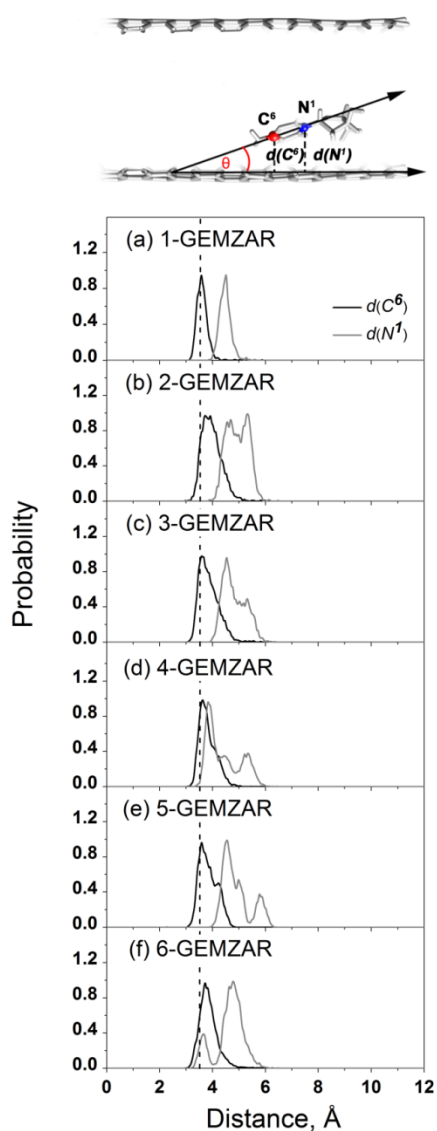
Figure 4.16 (Top) Schematic representation of the distances from the SWCNT surface to the C^6 and N^1 atoms of gemcitabine, $d(C^6)$ and $d(N^1)$, and the estimated angle, Θ, between the SWCNT vector from the C^6 to N^1 atoms of gemcitabine and the SWCNT parallel to inner surface. (Below) Distribution plot of the distances, $d(C^6)$ and $d(N^1)$, collected during the entire simulation period

are shown as black and grey lines, respectively, where the dashed line represents the $d(C^6)$ from the MP2/6-31G(d) optimization [96].

Therefore, a higher level of Θ fluctuation was a consequence of the presence of more than one gemcitabine molecule per SWCNT compared to that in 1-GEMZAR. This suggests the reduced strength of π-π stacking interactions between gemcitabine molecules and the SWCNT inner surface. In other words, the results clearly demonstrated that the loading of multiple encapsulated gemcitabine molecules inside each SWCNT decreased the drug binding interaction to its transporter.

Drug localization and interaction

Based on reference value of distance in cytosine pair, $d(Cr_i\text{-}Cr_j)$, of 4.3 Å [96], the five systems with number of gemcitabine >1 inside SWCNT can be classified into two groups. The first group (low drug loading) contained the 2-, 3- and 4- GEMZAR systems while the second high drug loading group was consisted of the 5- and 6- GEMZAR systems. For systems with a low drug uptake (less than ~21% w/v), the sharp and narrow peak of $d(Cr_i\text{-}Cr_j)$ with the most probable distance of 3.8-3.9 Å was considerably shorter than the reference value, as shown in Fig. 4.17(a-c). This indicates strong binding of the drug pair in which their cytosine rings oriented in a parallel-displace arrangement. Moreover, a few weak hydrogen bonds with an occupation percentage of <50% among drug molecules were found in these systems, as revealed in Fig. 4.17(f-h). A different situation occurred in a high drug uptake in the SWCNT hollow (5-GEMZAR and 6-GEMZAR), where the close contact between the gemcitabine molecules enhanced electrostatic interactions through strong hydrogen bonds, Fig. 4.17(d-e),while the π-π interaction between drug molecules cannot be recognized, shown as long $d(Cr_i\text{-}Cr_j)$ in Fig. 4.17(*i-j*). Hence, the staying in couple and keeping close to other drug molecules demonstrate that both

partial π-π interactions from cytosine rings and hydrogen bond interactions among drug themselves is an important factor in the localization of gemcitabines inside SWCNT.
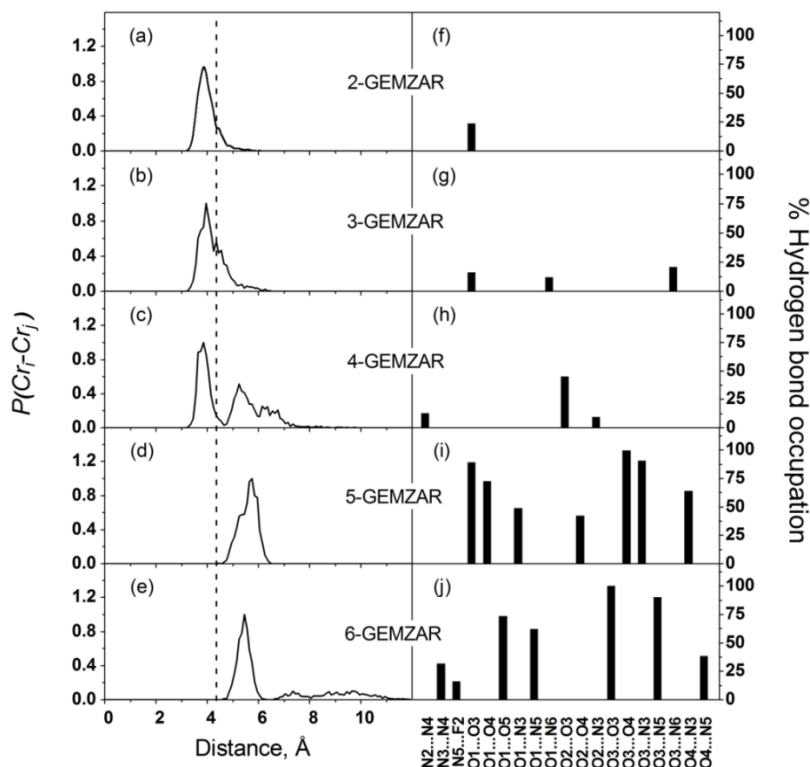
Figure 4.17 (Left) Probability of the averaged distances between the centers of the aromatic cytosine rings, $P(Cr_i\text{-}Cr_j)$, of the i-GEMZAR system where i is 2-6 in (a)-(e), respectively. The experimental $d[Cr_i\text{-}Cr_j]$ of 4.3 Å [96] is shown by the dashed line. (Right) Percent occupations of H-bond formation among drug molecules of the corresponding i-GEMZAR system where i is 2-6 are shown in (f)-(j), respectively.

4.4 The effect from length of chitosan linker to the conformation of EGF in targeted DDS

The results from REMD simulations of two systems different in number of chitosan units in the temperature range 300-455 K were discussed in term of energy surface, chitosan orientation and EGF conformation to evaluate the effect of chitosan length.

1. Energy surfaces

The two dimensional (2D) free-energy surfaces at the lowest temperature, 300 K, of the EGF/30CS/SWCNT/Gemzar and EGF/60CS/SWCNT/Gemzar systems are illustrated in Figs. 4.18a and 4.18b, respectively. The free-energies were calculated as a function of two order parameters, $F(x, y)$, as shown in Eq. 4.1:

$$F(x, y) = -k_B T \log P(x, y). \tag{4.1}$$

Here x is the distance between the centers of gravity of EGF and CNT, d[Cg(EGF)−Cg(CNT)], while y is the distance between the centers of gravity of the first and the last chitosan units for EGF/30CS/SWCNT/Gemzar and EGF/60CS/SWCNT/Gemzar, d[Cg(^{1st}CS)-Cg(^{30th}CS)], and d[Cg(^{1st}CS)-Cg(^{60th}CS)], respectively. Boltzmann constant is k_B while T is the temperature (K) and $P(x, y)$ is the probability of x, y parameter distribution.

For the EGF/30CS/SWCNT/Gemzar DDS, the potential energy surfaces calculated from REMD simulations with ff96/igb1 and ff96/igb5 shown in Figs. 4.18a1 and 4.18b1 are nearly in the same pattern: *(i)* the global minimum with the highest probability of finding located in a range of (17-22 Å, 17-22 Å) and (18-23Å, 13-18 Å); and *(ii)* the local minimum with the secondary probability of finding at (14-15 Å, 35-36 Å) and (15-18Å, 25-26Å). Meanwhile, the global minimum from ff03/igb5 result is positioned at (13-16 Å, 13-16 Å) with the four noticeable local minima (Fig. 4.18c1). Interestingly, all three simulations indicated that 30CS chain enfolded

tightly around the SWCNT pulling the EGF closer to center of the SWCNT as shown in Figs. 4.19a1-4.19c1. Although the distance between the two chitosan ends, $d[Cg(^{1st}CS)-Cg(^{30th}CS)]$, at initial state was 79 Å, the length dramatically shortened to be < 25 Å in all global minimum structures which is significantly less than the SWCNT length (34 Å). This implies that the 30 chitosan units were insufficient to cover the entire surface of the studied tube. On the other hands, the shortened $d[Cg(EGF)-Cg(CNT)]$ at the global minimum structure referred that the EGF was forced to locate closer to the tube due to the tightly enfolded 30CS chain.

At the initial structure of EGF/60CS/SWCNT/Gemzar DDS, the $d[Cg(EGF)-Cg(CNT)]$ was 91 Å while the $d[Cg(^{1st}CS)-Cg(^{60th}CS)]$ was 85 Å. Although the energy surface for the three simulations are likely different, the structure at global minimum obtained from the simulations with ff96/igb1 and ff96/igb5 was located nearly the same location at (48-53 Å, 67-75 Å in Fig. 4.18a2) and (50-55 Å, 73-77 Å in Fig. 4.18b2). In case of the simulation with ff03/igb5 (Fig. 4.18c2), the global minimum structure was placed at decreased $d[Cg(^{1st}CS)-Cg(^{60th}CS)]$ of 55-63 Å while the $d[Cg(EGF)-Cg(CNT)]$ was almost equal to that of the previous two systems (45-55 Å). It is a worth to note that the $d[Cg(^{1st}CS)-Cg(^{60th}CS)]$ of all global minimum structures was dramatically longer than the SWCNT length (34 Å), and thus it was completely wrapped over the tube surface, Figs. 4.19(a2-c2). In addition, the $d[Cg(EGF)-Cg(CNT)]$ values, 38-85 Å, of all simulated structures of the 60CS system, Figs. 4.18(a2-c2), were higher than a half tube length (17 Å) suggesting that EGF did not lay on tube surface, Figs. 4.19(a2-c2), in contrast to those of the 30CS system, 10-33 Å, Figs. 4.18(a1-c1) and Figs. 4.19(a1-c1).
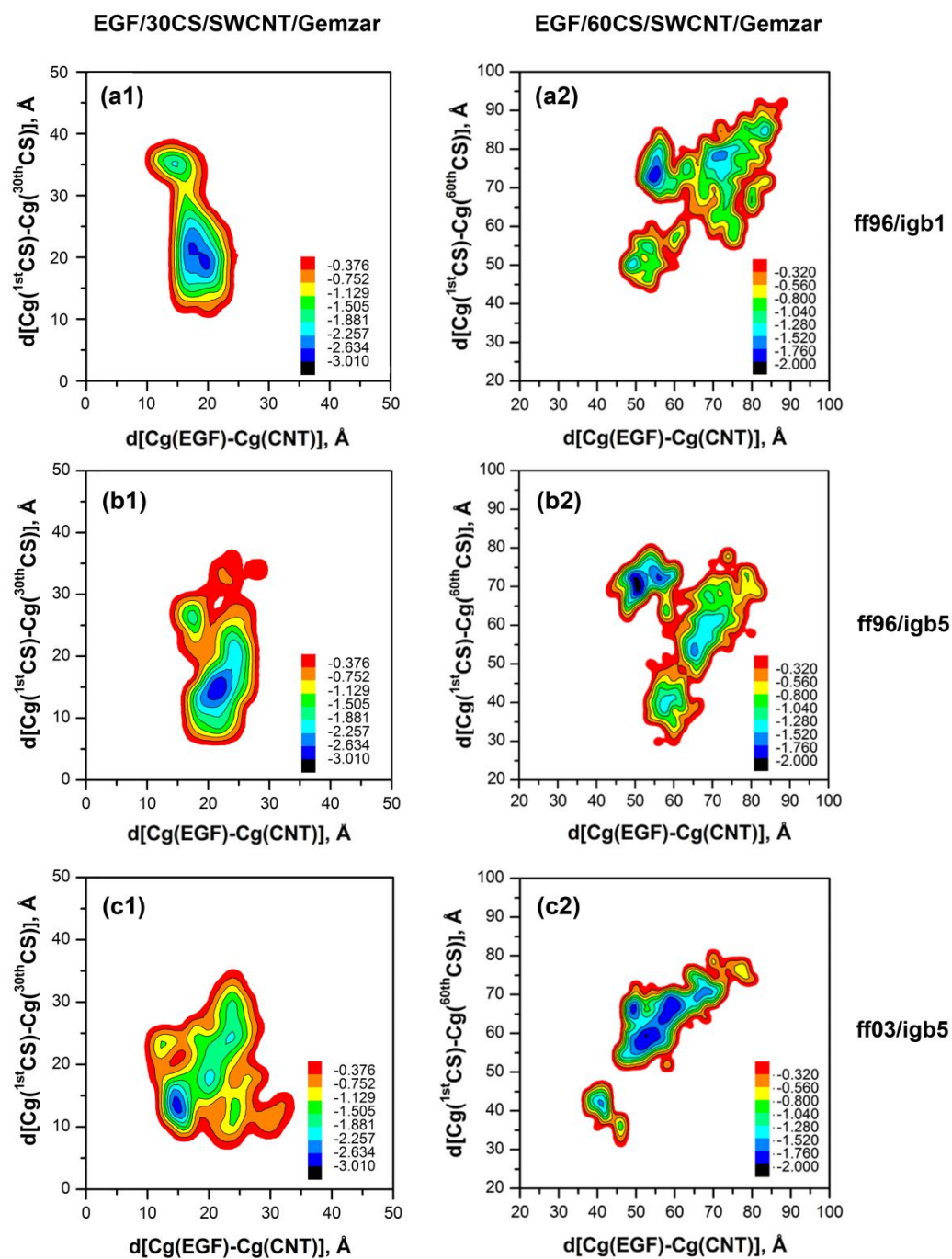
Figure 4.18 The 2D free-energy surfaces of the EGF/30CS/SWCNT/Gemzar and EGF/60CS/SWCNT/Gemzar DDSs at 300 K from REMD simulations with ff96/igb1, ff96/igb5 and ff03/igb5.
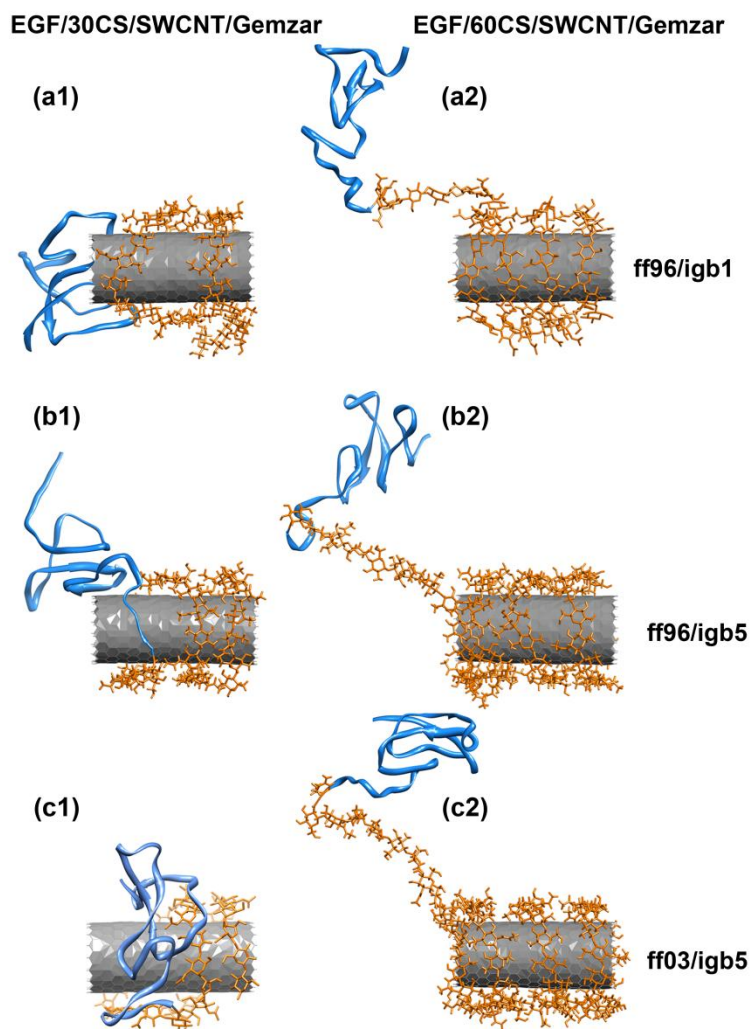
Figure 4.19 Representative schematic view for the global minimum structure of each REMD simulations with ff96/igb1, ff96/igb5 and ff03/igb5.

Chitosan orientation

At the initial state (Fig. 3.3 in page 23), only the first 10 chitosan units of the two DDS models (EGF/30CS/SWCNT/Gemzar and EGF/60CS/SWCNT/Gemzar DDSs) were freely situated outside the SWCNT surface, while the other 20 and 50 units in the EGF/30CS/SWCNT/Gemzar and EGF/60CS/SWCNT/Gemzar DDSs, respectively, were spirally enfolded around the SWCNT outer surface. After REMD simulations, the first 10 chitosan units

in the EGF/30CS/SWCNT/Gemzar system at 300 K moved to enfolding around SWCNT. As a result, all 30 chitosan units completely wrapped over SWCNT surface. Contrastingly, the first 10 chitosan units of EGF/60CS/SWCNT/Gemzar DDS are still located outside SWCNT surface while other 50 chitosan units, from 11th to 60th numbering of 60CS entirely wrapped around the SWCNT surface all the time, as shown in Fig. 4.20(c-d).
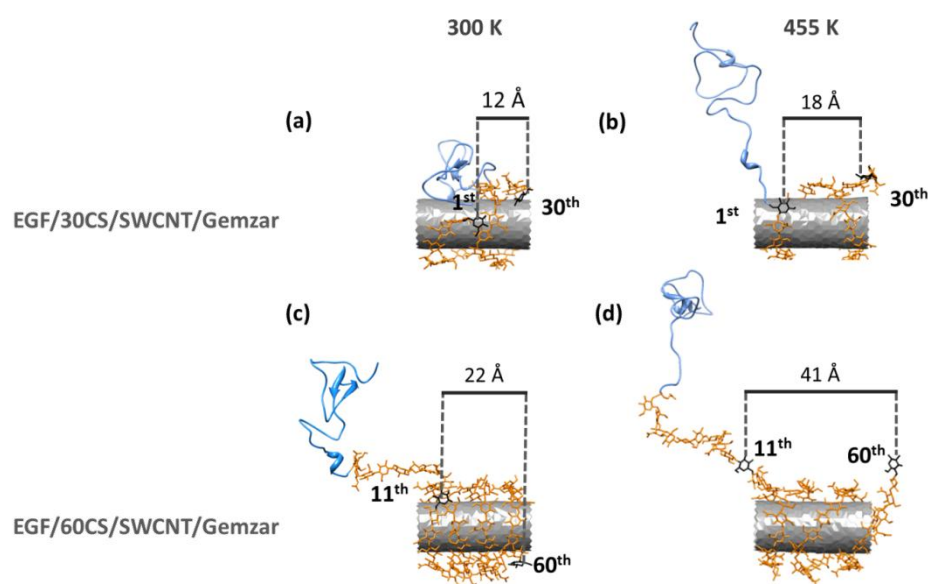
Figure 4.20 Schematic views of the $d_z[Cg(1^{st}CS)-Cg(30^{th}CS)]$ in the global minimum structure of the EGF/30CS/SWCNT/Gemzar DDS at (a) 300 and (b) 455 K, and the $d_z[^{Cg}(11thCS)-Cg(60^{th}CS)]$ in the global minimum structure of the EGF/60CS/SWCNT/Gemzar DDS at (c) 300 and (d) 455 K.

EGF conformation

To explore the effect of chitosan length to EGF conformation in two DDS systems, the secondary structures of EGF were investigated by using the DSSP algorithm [97] and presented in Fig. 4.21 with plots of β-sheet formational probability of each residue. Three implicit solvation sets, *i.e.*, ff96/igb1, ff96/igb5 and ff03/igb5, were also applied to compare the effect of

solvation model. Note that the *β*-sheet in the B-loop of EGF is significant for binding with EGFR [98]. According to the EGF crystal structure, the two major *β*-sheet formations locate at residues V19-I23 and K28-N32 while the other place nearby N terminal (S4-E5 and Y13-C14) and C terminal (Y37-I38 and Y44-R45) of the protein chain.
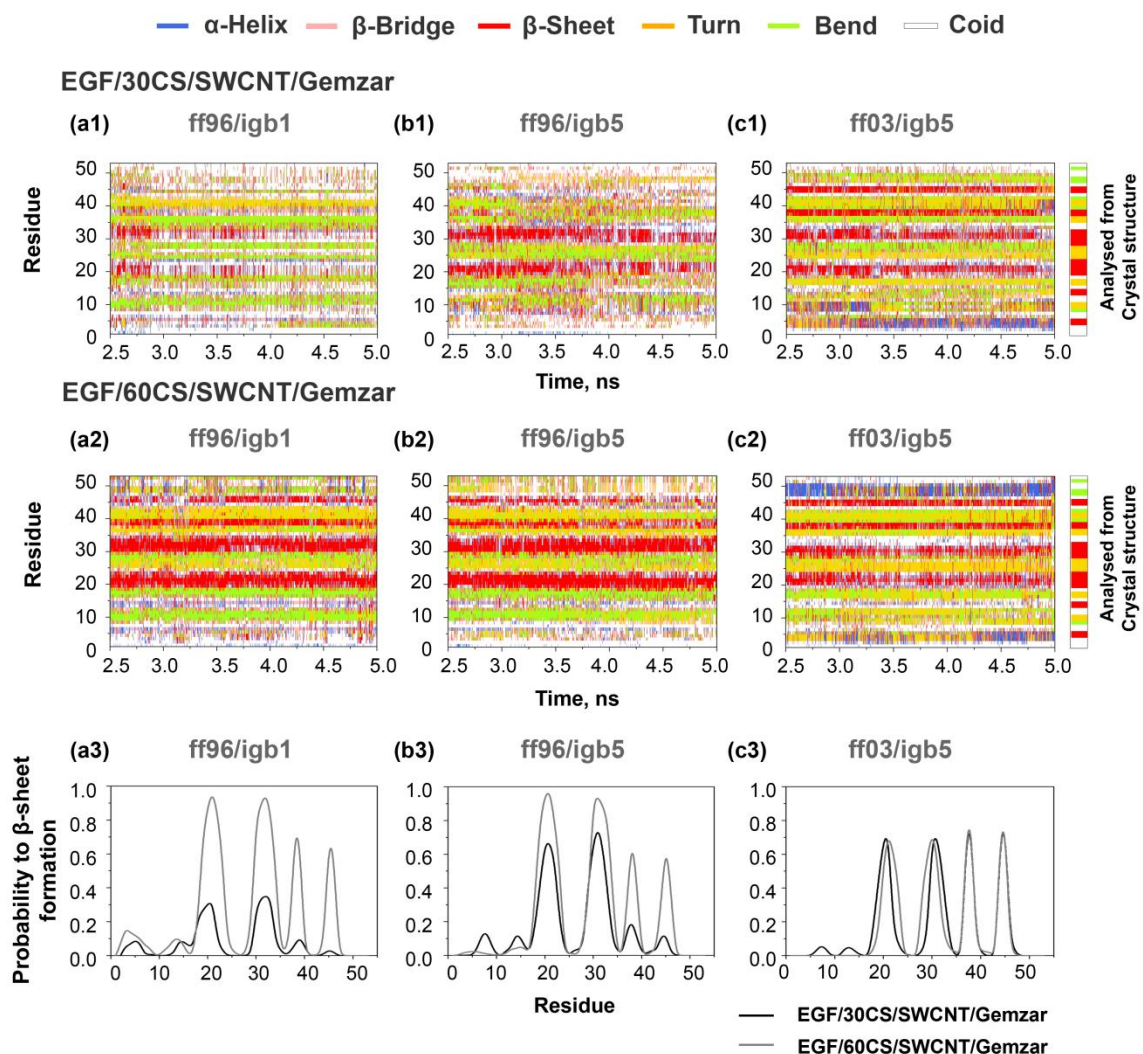
Figure 4.21 Secondary structure of EGF at 300 K obtained from the simulations of (a) the EGF/30CS/SWCNT/Gemzar DDS and (b) the EGF/60CS/SWCNT/Gemzar DDS. (c) The probability to form a β-sheet of each EGF residue where the grey regions represent the β-sheet from the crystal structure

For EGF/30CS/SWCNT/Gemzar DDS, the β-sheet formation at V19-I23 and K28-N32 is observed with 0.70 probability after REMD simulations using ff96/igb5 and ff03/ igb5 solvation models while the probability reduces noticeably in the simulation with ff96/igb1, shown as grey dash line in Figs. 4.21(a3-c3). In the EGF/60CS/SWCNT/Gemzar DDS, the major β-sheet regions firmly stable in the range of 0.70, 0.98 and 0.97 for the simulations with ff96/igb1, ff96/igb5 and ff03/igb5 as represented in red color in Figs. 4.21 (a2-c2) and black lines in Figs. 4.21 (a3-c3). In comparison with the EGF crystal structure, the preservation of β-sheets in residues V19-I23 and K28-N32 at the B-loop in EGF/60CS/SWCNT/Gemzar DDS systems is in agreement with the previous REMD simulation on pristine EGF [99]. Hence, the secondary structures of EGF is properly conserved only in the EGF/60CS/SWCNT/Gemzar DDS in which chitosan chain were long enough to wrap over SWCNT length.

(a) EGF/30CS/SWCNT/Gemzar

(b) EGF/60CS/SWCNT/Gemzar
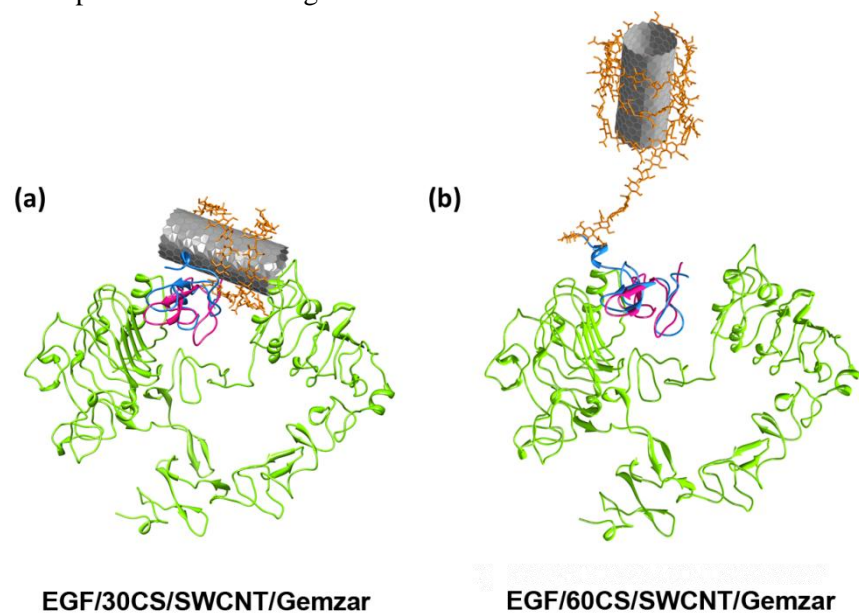
Figure 4.22 Superimposition on the EGF structures between the global minimum (blue) of (a) the EGF/30CS/SWCNT/Gemzar and (b) EGF/60CS/SWCNT/Gemzar DDSs and the co-crystal structure of EGF (pink)-EGFR (green).

From secondary structure analysis, EGF in EGF/30CS/SWCNT/Gemzar is not suitable to be effective DDS because the deformation of EGF secondary structure may affect to the binding with its receptor, EGFR. To evaluate the effect of chitosan length in DDS to the binding with EGFR, the global minimum structures of the DDS with 30 and 60 chitosan units obtained from the simulation with ff03/igb5 were superimposed on the crystal structure of the EGF-EGFR complex (pdb code 1NQL). It can be seen that only the EGF/60CS/SWCNT/Gemzar DDS was able to bind with EGFR without steric effects from SWCNT because EGF in this system was well aligned to the crystal EGF while the rest components of the DDS model are located outside the protein-protein binding region (Fig. 4.22b). Contrastingly, steric hindrance and undersigned contact between the SWCNT transporter of the EGF/30CS/SWCNT/Gemzar DDS and the EGFR were found (Fig. 4.22a) although there were 10 free chitosan units left outside the SWCNT surface to prevent such steric hindrance in the initial structure (Fig. 3.3a). In order to avoid the steric effect in the binding of EGF-EGFR (on cancer cells), the ratio of chitosan MW per SWCNT surface area should be larger than 9.9×10^{-7} kg/m^2, based upon the MW of 50 units of single layer chitosan per outer surface area of SWCNT with 14 Å in diameter and 34 Å in length in the present study.

Gemcitabine orientation

The displacement of gemcitabine drug inside SWCNT cavity at different temperatures for the two systems are explored in terms of the distance between center of gravity of gemcitabine and SWCNT surface, d[CNTsurface-Cg(drug)], as shown in Fig.10. Along REMD simulation in all temperatures, the gemcitabine always locates inside the SWCNT cavity with the distance in the range of -4.4 Å to -4.5 Å for both systems. Note that the negative charge of the d[CNTsurface-Cg(drug)] refers to its location inside the tube cavity. This distances are considerably shorter than that of the previous classical MD study on gemcitabine inside the

pristine SWCNT (4.7 Å) [77]. Therefore, the partial π-π interaction between cytosine ring of gemcitabine and surface of SWCNT can be formed. The average distances from the two systems at all temperatures are almost equal suggesting that the length of wrapped chitosan chain outside SWCNT surface did not involve the movement of drug inside the cavity.
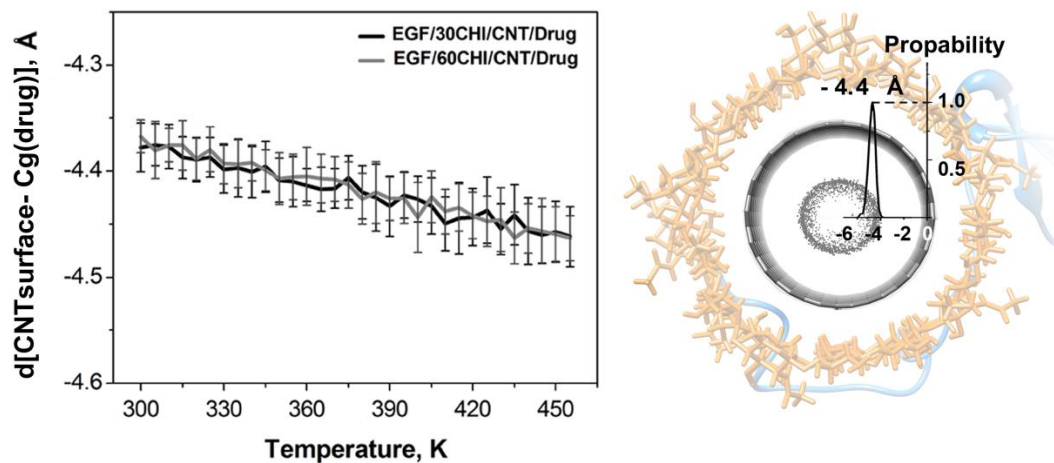
Figure 4.23. Temperature dependence of the distance between the center of gravity of gemcitabine and the SWCNT surface, d[CNTsurface-Cg(drug)]. The standard deviations are shown as vertical bars.

4.5 Binding interaction of targeted DDS with EGFR of cancer cell

The tether form of EGFR was selected to represent the inactive form of EGFR to investigate the binding interaction between EGF and EGFR. The MD simulations of two binding systems of EGF and EGFR with and without the presence of DDS, *i.e*., EGFR•EGF and EGFR•EGF-CS-SWCNT-Drug, were performed for 50 ns. To investigate the binding interaction of EGF and EGFR, the two systems were analyzed in terms of structure and energy.

System stability
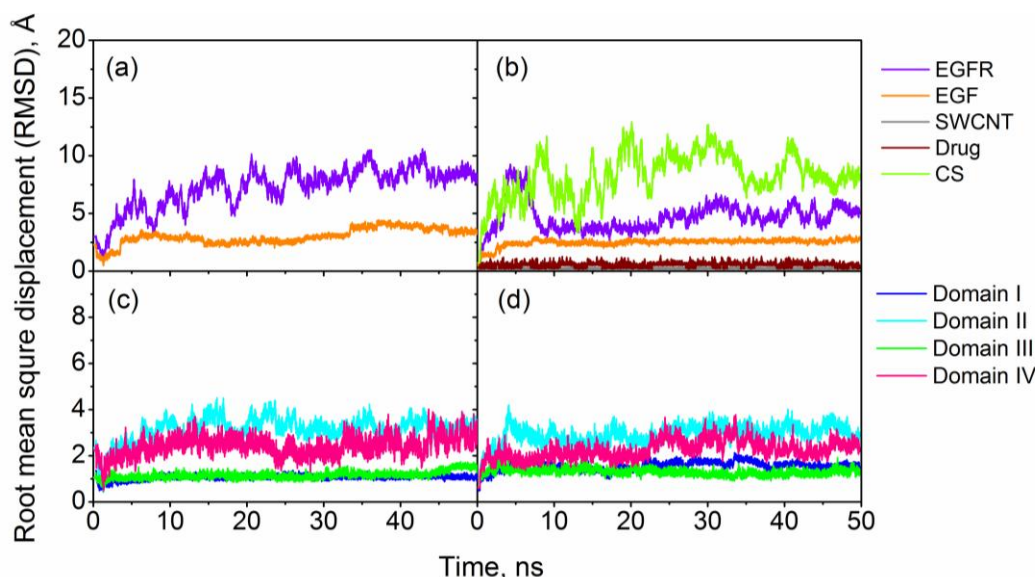
Figure 4.24 RMSDs relative to their initial structures for all heavy atoms in drug (brown), SWCNT (grey), chitosan, (light green) EGF (orange) and EGFR I-IV domains (blue, cyan, green and pink) for the EGFR•EGF and EGFR•EGF-CS-SWCNT-Drug systems.

To verify the stabilities of the two simulations, the root mean square displacement (RMSD) of all heavy atoms over the 50 ns MD simulation reverenced to their starting structures were plotted versus simulation time. The RMSDs of all fragments were given in the top row of Fig. 4.24, while those of EGFR four domains, domain I-IV, were separately displayed in bottom

of the same figure. Considering the EGFR protein, the RMSDs of the domain II (cyan) and IV (pink) of the three systems are relatively higher than those of domain I (blue) and III (green) that have RMSD value of 1Å . This is a consequence of the fact that domains I and III of EGFR form the stable six-turn right-hand β helix with hydrogen bonds between each stands, whilst domains II and IV are cysteine-rich domains having more degree of freedom from small disulfide bonds [32,45,100]. Although there were various different mixtures among the two studied systems, all systems reach their equilibrium state after 30 ns of MD simulation. Hence, the MD trajectories extracted from the 31-50 ns of simulations time were used for further analysis.

Intermolecular interaction of EGFR and EGF

        1. EGF in the pocket of EGFR

To examine the position of EGF in the binding pocket (between domain I and domain III) of EGFR, the distance from the N terminal of EGF to domain I and domain III, named d(N-domain I) and d(N-domain III), as well as the distance from C terminal to domain I and domain III of EGFR noted as d(C-domain I) and d(C-domain III), were plotted in Fig. 4.25.

In the pristine protein complex, EGFR•EGF, the d(N-domain I) and d(C-Domain I) are almost stable at 25 and 20 Å, respectively, while d(C-Domain III) was decreased from 31 Å to 14 Å after 30 ns of MD simulation and d(N-Domain III) fluctuated around 23-35 Å as shown in Fig.4.25a. This implies that the EGF in EGFR•EGF system moved a little bit closer to domain III while it kept contact with domain I of EGFR at the same time. The obtained results are in well agreement with the experimental study of ligand-induced dimerization process of EGFR [101]. For the system where chitosan acts as a linker between SWCNT and EGF, the d(N-Domain I) and d(C-Domain I) firmly stay around 21 and 25 Å, respectively, while d(N-Domain III) and d(C-Domain III) are of 27 and 6 Å, respectively as presented in Fig. 4.25(b). The dramatically shorten

of d(N-DomainIII), as shown in green line in Fig. 4.25(b), suggests the close contact of EGF to domain III of EGFR.
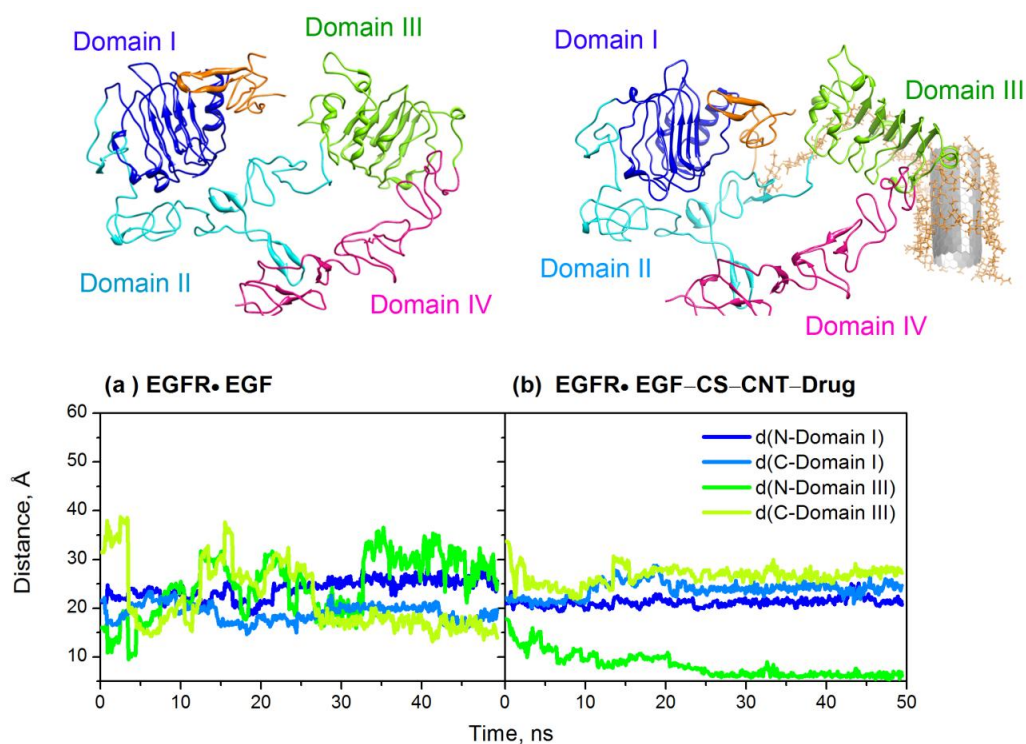
Figure 4.25 (Top) Schematic views of the last snapshots of (a) EGFR•EGF and (b) EGFR•EGF-CS-SWCNT-Drug systems. (Bottom) data plots of distances from end terminals of EGF to domain I and domain III of EGFR.

2. H-bond analysis

To insight into intermolecular interactions of EGFR and EGF, the percentages of hydrogen bond (H-bond) occupations between the two proteins in all two systems are summarized in Fig. 4.26.
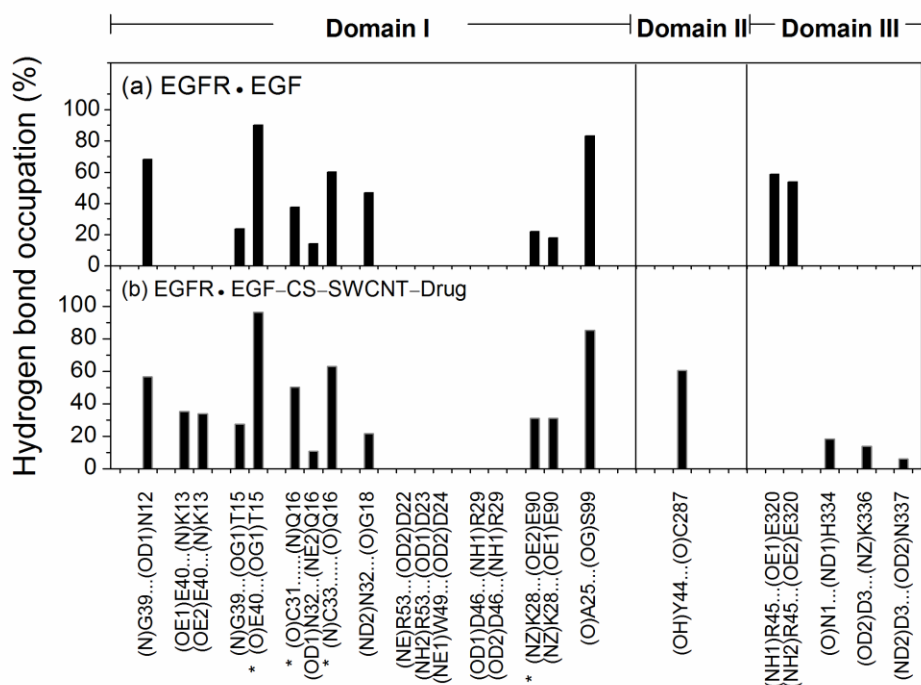
Figure 4.26 Percentage occupation of H-bond between EGFR and EGF of (a) EGFR•EGF and (b) EGFR•EGF-CS-SWCNT-Drug systems. The asterisk masks are denoted as hydrogen bond in the x-ray structure (PDB code: 1NQL).

For EGFR•EGF system, see Fig. 4.26(a), the intermolecular H-bonds between EGF and EGFR are not only occurred in domain I region which includes 4 H-bonds from the starting x-ray structure, (O)E40...(OG1)T15, (O)C31...(N)Q16, (N)C33...(O)Q16 and (NZ)K28...(OE2)E90 masked as asterisk in *x* axis of Fig. 4.26, but there are other H-bond formations in domain III as well. This implies that EGF moves closer to domain III and forms week H-bond with domain II and III of EGFR which is good agreement with the distance analysis from the previous section.

In the EGFR•EGF-CS-SWCNT-Drug system, the pattern of H-bond formation is almost the same as the EGFR•EGF system in which the H-bond occupation from EGF to domain I and domain III of EGFR were observed, shown in Fig. 4.26(b). Additionally, H-bonds between EGF

and domain III of EGFR were observed, *i.e.*, (O)N1...(ND1)H334, (OD2)D3...(NZ)K336 and (ND2)D3...(OD2)N337, as well as those with domain II of EGFR, *i.e.,* OH (OH)Y44...(O)C287, even the H-bond between R45 and E320 was not observed like in EGFR•EGF system.

The results from H-bond analysis confirm that there are interactions between EGF and domain I and domain III both in EGFR•EGF and EGFR•EGF-CS-SWCNT-Drug systems. Moreover, the patterns of the two systems are similarly suggesting that the binding efficiency of EGFR and EGF even EGF is coordinated with chitosan linker in DDS system.

3. Secondary structure analysis

The secondary structure of EGF and EGFR during 30-50 ns of MD simulations are analyzed by DSSP algorithm [97] to examine the conformation of the two proteins. It is clearly seen that the secondary structure of EGF in EGFR•EGF-CS-SWCNT-Drug is very identical with the crystal structure in which all six *β*-sheets from initial structure, S4-E5, Y13-C14, V19-I23, K28-N32, Y37-I38 and Y44-R45, were preserved as displayed as red color in Fig. 4.27(b). Therefore, the main secondary structures of EGF from the two systems were almost identical with the crystal structure.
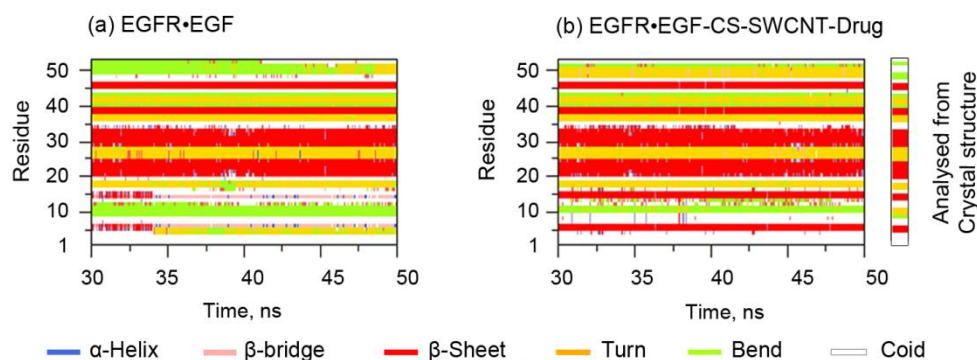
Figure 4.27 Secondary structure analysis of EGF in (a) EGFR•EGF and (b) EGFR•EGF-CS-SWCNT-Drug systems.
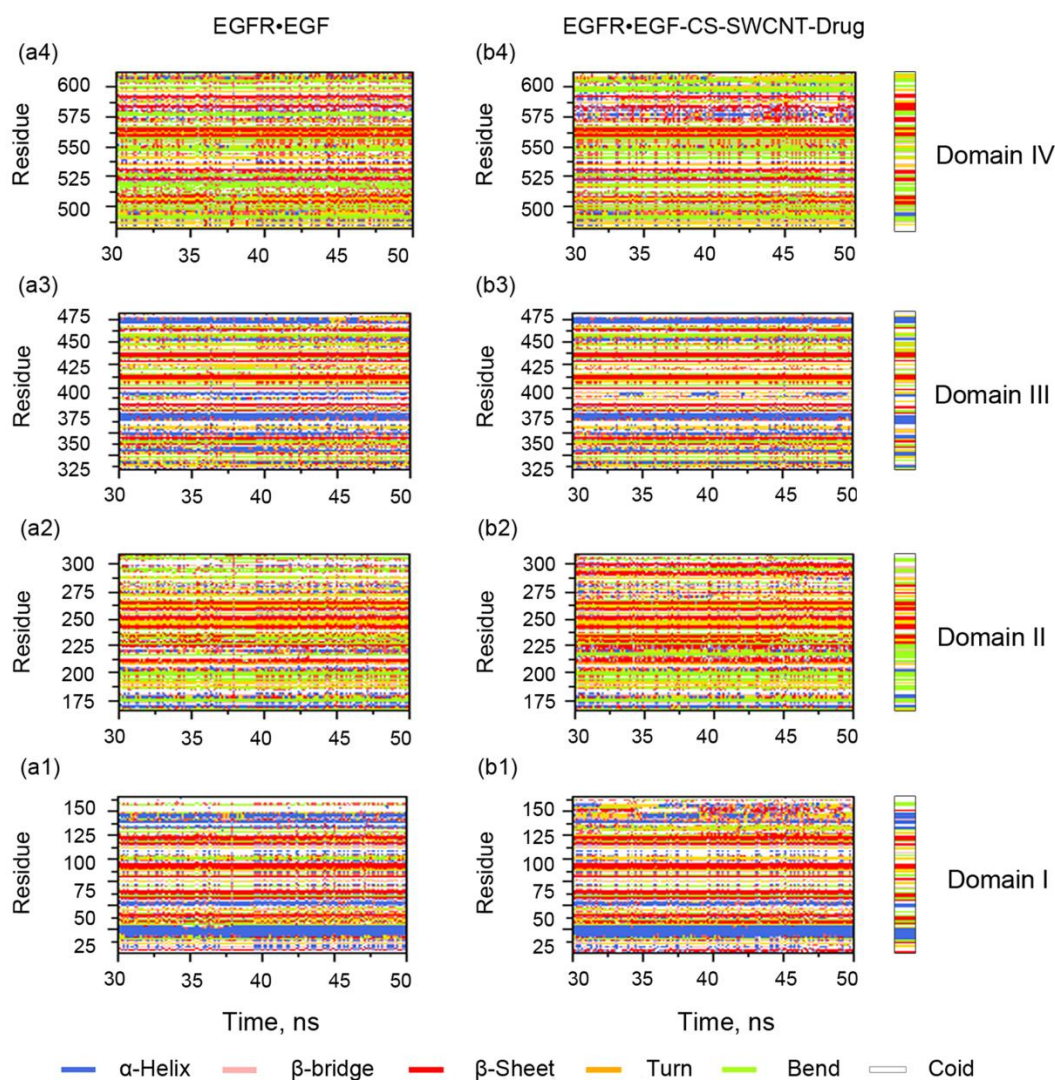
Figure 4.28 Secondary structure analysis of EGFR in (a) EGFR•EGF and (b) EGFR•EGF-CS-SWCNT-Drug systems.

The secondary structures of EGFR and percentage of β-sheet and α-helix of all 612 residues of EGFR are plotted in Fig. 4.28 and 4.29, respectively, where EGFR in the two studied systems appears to have similar secondary structure pattern except those in domain II region while β-sheet formation at 300-303 and 293-295 only observed in EGFR•EGF-CS-SWCNT-Drug. This implies that the DDS system did not interrupt the binding with EGFR because the

EGFR secondary structures in the binding complex with EGF and EGF-CS-SWCNT-Drug are very identical.
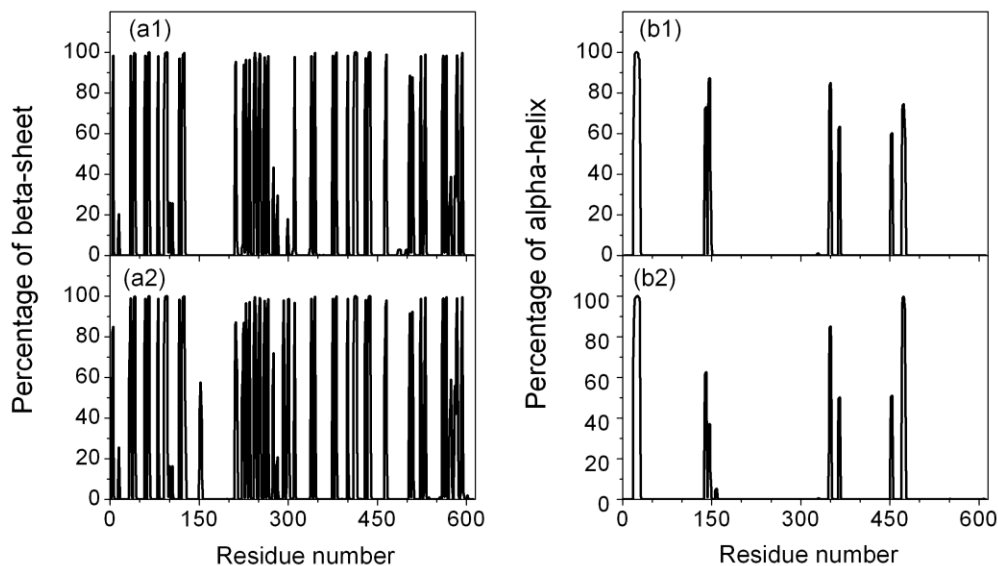
Figure 4.29 Percentage of *β*-sheets and *α*-helix formation of EGFR•EGF and EGFR•EGF-CS-SWCNT-Drug systems.

4. Binding energy analysis

The binding between EGFR and EGF in EGFR•EGF and EGFR•EGF-CS-SWCNT-Drug are calculated by MM/PBSA procedure which is successfully applied to several studies [77,102,103]. The obtained binding energies of the two systems are in the sequence of EGFR•EGF-CS-SWCNT-Drug > EGFR•EGF as shown details in Table. 4.7. When consider only EGF as ligand the binding energy is found to be closer with that obtained from wild type EGFR•EGF. Interestingly, when use the whole DDDS system as ligand is used, EGF-CS-SWCNT-Drug, the binding energy increases to -78.1 kcal/mol as shown in Table. 4.7. The outstanding binding energies in EGFR•EGF-CS-SWCNT-Drug systems over EGFR•EGF may result from the influence of chitosan in EGFR•EGF-CS-SWCNT-Drug system.

Table 4.7 The binding energies (in kcal/mol) between EGFR and pristine EGF as well as EGF in DDS systems

	EGFR•EGF	EGFR• EGF-CS-SWCNT-Drug	
		EGF as ligand	EGF-CS-SWCNT-Drug as ligand
ΔE_{ele}	-78.3 ± 44.4	-264.0 ± 54.1	-375.6 ± 56.7
ΔE_{vdW}	-84.1 ± 6.3	-101.2 ± 11.6	-171.0 ± 11.5
ΔE_{MM}	-162.4 ± 42.3	-365.2 ± 54.5	-546.6 ± 55.3
$\Delta G_{sol}^{nonpolar}$	-13.8 ± 0.8	-17.3 ± 1.3	-29.1 ± 1.2
ΔG_{sol}^{ele}	125.6 ± 38.4	330.2 ± 47.6	497.6 ± 54.3
ΔG_{sol}	111.8 ± 38.3	312.9 ± 47.0	468.5 ± 53.7
$\Delta G_{sol}^{ele} + \Delta E_{ele}$	47.3 ± 9.4	66.2 ± 10.3	122.0 ± 9.6
$\Delta G_{sol}^{nonpolar} + \Delta E_{vdW}$	-98.8 ± 7.2	-118.4 ± 12.8	-200.2 ± 12.7
ΔG_{bind}	**-50.6 ± 7.6**	**-52.3 ± 11.2**	**-78.1 ± 11.4**
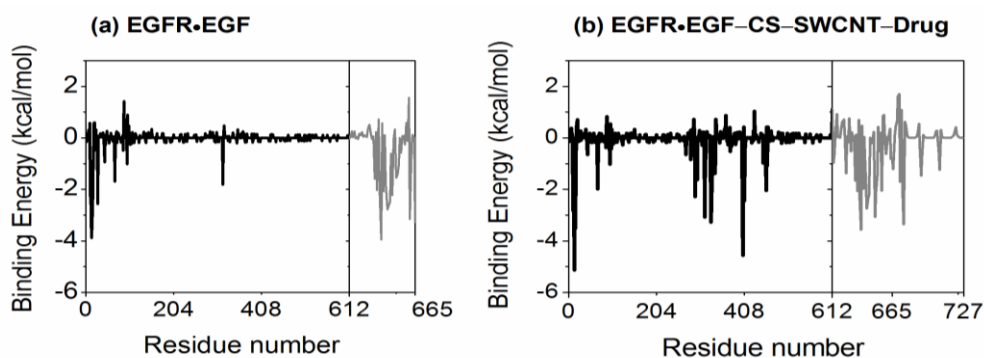
Figure 4.30 Energy decomposition of (a) EGFR•EGF and (b) EGFR•EGF-CS-SWCNT-Drug systems.

To confirm the contribution of components in DDS conjugated EGF to the binding interaction with EGFR, energy decompositions of the two systems are calculated by using DC module of MM/PBSA. The contribution of each sequence number is presented in Fig. 4.30. In

EGFR•EGF complex, the binding energy between EGFR and EGF comes from residue E3 to S99 of domain I and residue E320 of domain III in EGFR with residue 632-665 (H10 -R53) of EGF. In EGFR•EGF-CS-SWCNT-Drug, there are many residues in domain I (residue 1-615) and especially domain III (residue 310-481) contributing to the binding with EGF more than those observed in the wild type systems. Besides, the main contributions of binding energies did not only come from of EGFR (residue 1-612) and most residues of EGF (613-665) but from the first 10 units of chitosan chain (residue 666-675) that exist freely outside SWCNT surface and also stabilizes the binding with EGFR. For that reason, the stabilities of EGFR and DDS conjugated EGF complexes come from both of interaction among proteins themselves (EGF and EGFR) and DDS component (chitosan and SWCNT). In conclusion, all the results confirm that the EGF in conjugate with DDS in EGFR•EGF-CS-SWCNT-Drug have similar binding pattern with the wild type complex of EGF and EGFR. Thus, the EGF-CS-SWCNT-Drug can be a successful candidate for target DDS system for cancer therapy.

CHAPTER V
CONCLUSION

In the present study, computational techniques have been applied to understand the interaction of anti-cancer drugs with carbon nanomaterials carrier as well as the interaction of the targeted DDS to the binding with receptor of cancer cell. The scope of the study is divided into five parts, *i.e.,* i) Investigation of the arrangement of doxorubicin over graphene, ii) non-covalent interaction of nucleic acid analogue anti-cancer drug with graphene, iii) gemcitabine anti-cancer drug loading capacity in carbon nanotube cavity, iv) the effect of chitosan length in targeted DDS and, v) the last one, binding of targeted DDS to the receptor of cancer cell.

For the first two parts, DFTB and DFT calculations of the interactions between anti-cancer drugs and graphene showed that the drug orienting parallel to aromatic surface plane of graphene stabilized the π-π stacking interaction. In addition, larger aromatic system of the drug leaded to higher stability of the complexes.

In the third part, the MD simulations of various numbers of gemcitabine anti-cancer drugs inside CNT were performed to evaluate the capacity of drug loading inside CNT, The results suggest that both π-π stacking interaction between the aromatic cytosine ring of gemcitabine and interactions among drugs themselves influence the drug orientations inside CNT cavities. The results from the first three parts confirm that CNT and graphene can be served as a proper carrier for anti-cancer drug containing aromatic conjugates.

For the fourth session, the conformation of the two DDS system different in length (30 or 60 units length) of wrapped chitosan over CNT have been performed by REMD simulations at temperatures ranging from 300 to 455 K. The results point out that a close packing of chitosan

orbit around the SWCNT in the system with short chitosan length, EGF/30CS/SWCNT/Gemzar DDS imposed EGF to relocate close to the tube surface, and thus, the steric hindrance induced by chitosan and the SWCNT may block the binding of EGF onto the EGFR. Therefore, chitosan chain wrapped around the SWCNT should be long enough to cover the entire SWCNT surface.

In the last part, the binding of DDS contained EGF as targeting agent with receptor of cancer cell, EGFR, has been explored by using classic MD simulation. The result is in agreement with the REMD simulation in which EGF connected to SWCNT via 60 units chitosan chain is a good candidate for targeted DDS, due to the binding of EGF with EGFR was not interrupted by DDS components and the behavior of EGF in this DDS system is similar with pristine EGF in term of binding affinity with EGFR.

Taken altogether, all the results from several computational techniques confirm that carbon nanomaterials such as graphene and SWCNT can be used as anti-cancer drug carriers and can be modified to increasing specificity toward cancer cell by attaching with targeting agent. Furthermore, the DDS based on CNT can be designed to prevent the steric effect to the binding with cancer cell receptor by using appropriated length of chitosan linker. The obtained results fulfill not only the better understanding of DDS but also worthwhile to the design of successful targeted DDS in the near future.

REFERENCES

[1]   Rosen, H. and Abribat, T. The rise and rise of drug delivery. Nature Reviews
        Drug Discovery 4 (2005): 381-385.

[2]   Novoselov, K. S., Geim, A. K., Morozov, S. V., Jiang, D., Zhang, Y., et al.
        Electric field effect in atomically thin carbon films. Science 306 (2004):
        666-669.

[3]   Panigrahi, S., Bhattacharya, A., Banerjee, S. and Bhattacharyya, D. Interaction of
        Nucleobases with Wrinkled Graphene Surface: Dispersion Corrected DFT
        and AFM Studies. The Journal of Physical Chemistry C 116 (2012): 4374-
        4379.

[4]   Husale, S., Sahoo, S., Radenovic, A., Traversi, F., Annibale, P., et al. ssDNA
        Binding Reveals the Atomic Structure of Graphene. Langmuir 26 (2010):
        18078-18082.

[5]   Liu, F., Choi, J. Y. and Seo, T. S. DNA mediated water-dispersible graphene
        fabrication   and   gold   nanoparticle-graphene   hybrid.   Chemical
        Communications 46 (2010): 2844-2846.

[6]   Liu, Z., Robinson, J. T., Sun, X. and Dai, H. PEGylated Nanographene Oxide for
        Delivery of Water-Insoluble Cancer Drugs. Journal of the American
        Chemical Society 130 (2008): 10876-10877.

[7]   Lu, C.H., Zhu, C.L., Li, J., Liu, J.J., Chen, X., et al. Using graphene to protect
        DNA from cleavage during cellular delivery. Chemical Communications
        46 (2010): 3116-3118.

[8]   Ramraj, A., Hillier, I. H., Vincent, M. A. and Burton, N. A. Assessment of
        approximate quantum chemical methods for calculating the interaction
        energy of nucleic acid bases with graphene and carbon nanotubes.
        Chemical Physics Letters 484 (2010): 295-298.

[9]   Antony, J. and Grimme, S. Structures and interaction energies of stacked
        graphene-nucleobase complexes. Physical Chemistry Chemical Physics 10
        (2008): 2722-2729.

[10]   Iijima, S. Helical microtubules of graphitic carbon. Nature 354 (1991): 56-58.

[11]   Sinnott, S. B. and Andrews, R. Carbon nanotubes: Synthesis, properties, and
        applications. Critical Reviews in Solid State and Materials Sciences 26
        (2001): 145-249.

[12]   Dai, H. Carbon Nanotubes: Synthesis, Integration, and Properties. <u>Accounts of Chemical Research</u> 35 (2002): 1035-1044.

[13]   Lu, X. and Chen, Z. Curved Pi-Conjugation, Aromaticity, and the Related Chemistry of Small Fullerenes (<C60) and Single-Walled Carbon Nanotubes. <u>Chemical Reviews</u> 105 (2005): 3643-3696.

[14]   Avouris, P. Carbon nanotube electronics. <u>Chemical Physics</u> 281 (2002): 429-445.

[15]   Foldvari, M. and Bagonluri, M. Carbon nanotubes as functional excipients for nanomedicines: I. pharmaceutical properties. <u>Nanomedicine-Nanotechnology Biology and Medicine</u> 4 (2008): 173-182.

[16]   Liu, Z., Tabakman, S. M., Chen, Z. and Dai, H. J. Preparation of carbon nanotube bioconjugates for biomedical applications. <u>Nature Protocols</u> 4 (2009): 1372-1382.

[17]   Liu, J., Bibari, O., Mailley, P., Dijon, J., Rouviere, E., et al. Stable non-covalent functionalisation of multi-walled carbon nanotubes by pyrene-polyethylene glycol through pi-pi stacking. <u>New Journal of Chemistry</u> 33 (2009): 1017-1024.

[18]   Hong, H., Gao, T. and Cai, W. Molecular imaging with single-walled carbon nanotubes. <u>Nano Today</u> 4 (2009): 252-261.

[19]   Xu, J. X., Yudasaka, M., Kouraba, S., Sekido, M., Yamamoto, Y., et al. Single wall carbon nanohorn as a drug carrier for controlled release. <u>Chemical Physics Letters</u> 461 (2008): 189-192.

[20]   Prato, M., Kostarelos, K. and Bianco, A. Functionalized Carbon Nanotubes in Drug Design and Discovery. <u>Accounts of Chemical Research</u> 41 (2007): 60-68.

[21]   Liu, Z., Chen, K., Davis, C., Sherlock, S., Cao, Q. Z., et al. Drug delivery with carbon nanotubes for in vivo cancer treatment. <u>Cancer Research</u> 68 (2008): 6652-6660.

[22]   Pastorin, G. Crucial Functionalizations of Carbon Nanotubes for Improved Drug Delivery: A Valuable Option? <u>Pharmaceutical Research</u> 26 (2009): 746-769.

[23]   Wu, W., Li, R., Bian, X., Zhu, Z., Ding, D., et al. Covalently Combining Carbon Nanotubes with Anticancer Agent: Preparation and Antitumor Activity. <u>Acs Nano</u> 3 (2009): 2740-2750.

[24] Ajima, K., Yudasaka, M., Murakami, T., Maigne, A., Shiba, K., et al. Carbon nanohorns as anticancer drug carriers. Molecular Pharmaceutics 2 (2005): 475-480.

[25] Liu, Z., Fan, A. C., Rakhra, K., Sherlock, S., Goodwin, A., et al. Supramolecular Stacking of Doxorubicin on Carbon Nanotubes for In Vivo Cancer Therapy. Angewandte Chemie-International Edition 48 (2009): 7668-7672.

[26] Ovaa, H., Kuijl, C. and Neefjes, J. Recent and new targets for small molecule anti-cancer agents. Drug Discovery Today: Technologies 6 (2009): e3-e11.

[27] Heister, E., Neves, V., Tilmaciu, C., Lipert, K., Beltrán, V. S., et al. Triple functionalisation of single-walled carbon nanotubes with doxorubicin, a monoclonal antibody, and a fluorescent marker for targeted cancer therapy. Carbon 47 (2009): 2152-2160.

[28] Zhang, X. K., Meng, L. J., Lu, Q. G., Fei, Z. F. and Dyson, P. J. Targeted delivery and controlled release of doxorubicin to cancer cells using modified single wall carbon nanotubes. Biomaterials 30 (2009): 6041-6047.

[29] Wang, Y., Yang, S.-T., Wang, Y., Liu, Y. and Wang, H. Adsorption and desorption of doxorubicin on oxidized carbon nanotubes. Colloids and Surfaces B: Biointerfaces 97 (2012): 62-69.

[30] Sornmee, P., Rungrotmongkol, T., Saengsawang, O., Arsawang, U., Remsungnen, T., et al. Understanding the Molecular Properties of Doxorubicin Filling Inside and Wrapping Outside Single-Walled Carbon Nanotubes. Journal of Computational and Theoretical Nanoscience 8 (2011): 1385-1391.

[31] Patel, M. P., Patel, R. R. and Patel, J. K. Chitosan Mediated Targeted Drug Delivery System: A Review. Journal of Pharmacy and Pharmaceutical Sciences 13 (2010): 536-557.

[32] Park, J. H., Saravanakumar, G., Kim, K. and Kwon, I. C. Targeted delivery of low molecular drugs using chitosan and its derivatives. Advanced Drug Delivery Reviews 62 (2010): 28-41.

[33] Rana, V. K., Choi, M. C., Kong, J. Y., Kim, G. Y., Kim, M. J., et al. Synthesis and Drug-Delivery Behavior of Chitosan-Functionalized Graphene Oxide Hybrid Nanosheets. Macromolecular Materials and Engineering 296 (2011): 131-140.

[34] Sahu, S. K., Maiti, S., Maiti, T. K., Ghosh, S. K. and Pramanik, P. Hydrophobically modified carboxymethyl chitosan nanoparticles targeted delivery of paclitaxel. Journal of Drug Targeting 19 (2011): 104-113.

[35] Galbiati, A., Tabolacci, C., Della Rocca, B. M., Mattioli, P., Beninati, S., et al. Targeting Tumor Cells through Chitosan-Folate Modified Microcapsules Loaded with Camptothecin. Bioconjugate Chemistry 22 (2011): 1066-1072.

[36] Rungrotmongkol, T., Arsawang, U., Iamsamai, C., Vongachariya, A., Dubas, S. T., et al. Increased dispersion and solubility of carbon nanotubes noncovalently modified by the polysaccharide biopolymer, chitosan: MD simulations. Chemical Physics Letters 507 (2011): 134-137.

[37] Iamsamai, C., Hannongbua, S., Ruktanonchai, U., Soottitantawat, A. and Dubas, S. T. The effect of the degree of deacetylation of chitosan on its dispersion of carbon nanotubes. Carbon 48 (2010): 25-30.

[38] Normanno, N., De Luca, A., Bianco, C., Strizzi, L., Mancino, M., et al. Epidermal growth factor receptor (EGFR) signaling in cancer. Gene 366 (2006): 2-16.

[39] Nielsen, J. S., Jakobsen, E., HØlund, B., Bertelsen, K. and Jakobsen, A. Prognostic significance of p53, Her-2, and EGFR overexpression in borderline and epithelial ovarian cancer. International Journal of Gynecological Cancer 14 (2004): 1086-1096.

[40] Hartmann, L. C., Keeney, G. L., Lingle, W. L., Christianson, T. J. H., Varghese, B., et al. Folate receptor overexpression is associated with poor outcome in breast cancer. International Journal of Cancer 121 (2007): 938-942.

[41] Liang, F. and Chen, B. A Review on Biomedical Applications of Single-Walled Carbon Nanotubes. Current Medicinal Chemistry 17 (2010): 10-24.

[42] Lax, I., Bellot, F., Howk, R., Ullrich, A., Givol, D., et al. Functional analysis of the ligand binding site of EGF-receptor utilizing chimeric chicken/human receptor molecules. The EMBO Journal 8 (1989): 421-427.

[43] Ogiso, H., Ishitani, R., Nureki, O., Fukai, S., Yamanaka, M., et al. Crystal Structure of the Complex of Human Epidermal Growth Factor and Receptor Extracellular Domains. Cell 110 (2002): 775-787.

[44] Ferguson, K. M., Berger, M. B., Mendrola, J. M., Cho, H.-S., Leahy, D. J., et al. EGF Activates Its Receptor by Removing Interactions that Autoinhibit Ectodomain Dimerization. Molecular Cell 11 (2003): 507-517.

[45]   Burgess, A. W., Cho, H.-S., Eigenbrot, C., Ferguson, K. M., Garrett, T. P. J., et al. An Open-and-Shut Case? Recent Insights into the Activation of EGF/ErbB Receptors. <u>Molecular Cell</u> 12 (2003): 541-552.

[46]   Press, M. and Lenz, H.-J. EGFR, HER2 and VEGF Pathways. <u>Drugs</u> 67 (2007): 2045-2075.

[47]   Lurje, G. and Lenz, H. J. EGFR Signaling and Drug Discovery. <u>Oncology</u> 77 (2009): 400-410.

[48]   Li, S., Schmitz, K. R., Jeffrey, P. D., Wiltzius, J. J. W., Kussie, P., et al. Structural basis for inhibition of the epidermal growth factor receptor by cetuximab. <u>Cancer Cell</u> 7 (2005): 301-311.

[49]   Holbro, T. and Hynes, N. E. ERBB RECEPTORS: Directing Key Signaling Networks Throughout Life. <u>Annual Review of Pharmacology and Toxicology</u> 44 (2004): 195-217.

[50]   Dawson, J. P., Bu, Z. and Lemmon, M. A. Ligand-Induced Structural Transitions in ErbB Receptor Extracellular Domains. <u>Structure</u> 15 (2007): 942-954.

[51]   Acharya, S., Dilnawaz, F. and Sahoo, S. K. Targeted epidermal growth factor receptor nanoparticle bioconjugates for breast cancer therapy. <u>Biomaterials</u> 30 (2009): 5737-5750.

[52]   Tseng, C. L., Wu, S. Y. H., Wang, W. H., Peng, C. L., Lin, F. H., et al. Targeting efficiency and biodistribution of biotinylated-EGF-conjugated gelatin nanoparticles administered via aerosol delivery in nude mice with lung cancer. <u>Biomaterials</u> 29 (2008): 3014-3022.

[53]   Yang, L. L., Mao, H., Wang, Y. A., Cao, Z. H., Peng, X. H., et al. Single Chain Epidermal Growth Factor Receptor Antibody Conjugated Nanoparticles for in vivo Tumor Targeting and Imaging. <u>Small</u> 5 (2009): 235-243.

[54]   Mendelsohn, J. The epidermal growth factor receptor as a target for cancer therapy. <u>Endocrine-Related Cancer</u> 8 (2001): 3-9.

[55]   Bhirde, A. A., Patel, V., Gavard, J., Zhang, G. F., Sousa, A. A., et al. Targeted Killing of Cancer Cells in Vivo and in Vitro with EGF-Directed Carbon Nanotube-Based Drug Delivery. <u>ACS Nano</u> 3 (2009): 307-316.

[56]   Thomas, L. H. The calculation of atomic fields. <u>Mathematical Proceedings of the Cambridge Philosophical Society</u> 23 (1927): 542-548.

[57]   Hohenberg, P. and Kohn, W. Inhomogeneous Electron Gas. <u>Physical Review</u> 136 (1964): B864-B871.

[58]   Grimme, S. Density functional theory with London dispersion corrections. <u>Wiley Interdisciplinary Reviews: Computational Molecular Science</u> 1 (2011): 211-228.

[59]   Zhao, Y. and Truhlar, D. G. Density Functionals with Broad Applicability in Chemistry. <u>Accounts of Chemical Research</u> 41 (2008): 157-167.

[60]   Zhao, Y. and Truhlar, D. The M06 suite of density functionals for main group thermochemistry, thermochemical kinetics, noncovalent interactions, excited states, and transition elements: two new functionals and systematic testing of four M06-class functionals and 12 other functionals. <u>Theoretical Chemistry Accounts</u> 120 (2008): 215-241.

[61]   Schneider, R., Sharma, A. and Rai, A. (2008) Introduction to Molecular Dynamics; Fehske H, Schneider R, Weiße A, editors: Springer Berlin Heidelberg. 3-40 p.

[62]   Sugita, Y. and Okamoto, Y. Replica-exchange molecular dynamics method for protein folding. <u>Chemical Physics Letters</u> 314 (1999): 141-151.

[63]   Hukushima, K. and Nemoto, K. Exchange Monte Carlo Method and Application to Spin Glass Simulations. <u>Journal of the Physical Society of Japan</u> 65 (1996): 1604-1608.

[64]   Mitsutake, A., Sugita, Y. and Okamoto, Y. Generalized-ensemble algorithms for molecular simulations of biopolymers. <u>Peptide Science</u> 60 (2001): 96-123.

[65]   Nymeyer, H., Gnanakaran, S. and García, A. E. Atomic Simulations of Protein Folding, Using the Replica Exchange Algorithm. <u>Methods in Enzymology</u> 383 (2004): 119-149.

[66]   Cheng, X., Cui, G., Hornak, V. and Simmerling, C. Modified Replica Exchange Simulation Methods for Local Structure Refinement. <u>Journal of Physical Chemistry B</u> 109 (2005): 8220-8230.

[67]   Hansmann, U. H. E. Parallel tempering algorithm for conformational studies of biological molecules. <u>Chemical Physics Letters</u> 281 (1997): 140-150.

[68]   Civcir, P. U. Tautomerism of 6-thioguanine in the gas and aqueous phases using AM1 and PM3 methods. <u>Journal of Molecular Structure: THEOCHEM</u> 536 (2001): 161-171.

[69]   Szeghalmi, A. V., Leopold, L., Pînzaru, S., Chis, V., Silaghi-Dumitrescu, I., et al. Adsorption of 6-mercaptopurine and 6-mercaptopurine riboside on silver colloid: a pH dependent surface enhanced Raman spectroscopy and

density functional theory study. Part I. 6-Mercaptopurine. <u>Journal of Molecular Structure</u> 735–736 (2005): 103-113.

[70]   Latosińska, J. N., Seliger, J., Žagar, V. and Burchardt, D. V. Hydrogen Bonding and Stacking $\pi-\pi$ Interactions in Solid 6-Thioguanine and 6-Mercaptopurine (Antileukemia and Antineoplastic Drugs) Studied by NMR-NQR Double Resonance Spectroscopy and Density Functional Theory. <u>The Journal of Physical Chemistry A</u> 113 (2009): 8781-8790.

[71]   Elstner, M., Porezag, D., Jungnickel, G., Elsner, J., Haugk, M., et al. Self-consistent-charge density-functional tight-binding method for simulations of complex materials properties. <u>Physical Review B</u> 58 (1998): 7260-7268.

[72]   Wishart, D. S., Knox, C., Guo, A. C., Shrivastava, S., Hassanali, M., et al. DrugBank: a comprehensive resource for in silico drug discovery and exploration. <u>Nucleic Acids Research</u> 34 (2006): D668-D672.

[73]   Elstner, M., Hobza, P., Frauenheim, T., Suhai, S. and Kaxiras, E. Hydrogen bonding and stacking interactions of nucleic acid base pairs: A density-functional-theory based treatment. <u>The Journal of Chemical Physics</u> 114 (2001): 5149-5155.

[74]   Aradi, B., Hourahine, B. and Frauenheim, T. DFTB+, a Sparse Matrix-Based Implementation of the DFTB Method†. <u>The Journal of Physical Chemistry A</u> 111 (2007): 5678-5684.

[75]   Sabini, E., Hazra, S., Konrad, M. and Lavie, A. Nonenantioselectivity Property of Human Deoxycytidine Kinase Explained by Structures of the Enzyme in Complex with L- and D-Nucleosides. <u>Journal of Medicinal Chemistry</u> 50 (2007): 3004-3014.

[76]   Duan, Y., Wu, C., Chowdhury, S., Lee, M. C., Xiong, G., et al. A point-charge force field for molecular mechanics simulations of proteins based on condensed-phase quantum mechanical calculations. <u>Journal of Computational Chemistry</u> 24 (2003): 1999-2012.

[77]   Arsawang, U., Saengsawang, O., Rungrotmongkol, T., Sornmee, P., Wittayanarakul, K., et al. How do carbon nanotubes serve as carriers for gemcitabine transport in a drug delivery system? <u>Journal of Molecular Graphics and Modelling</u> 29 (2011): 591-596.

[78]   Ferrari, A. M., Degliesposti, G., Sgobba, M. and Rastelli, G. Validation of an automated procedure for the prediction of relative free energies of binding on a set of aldose reductase inhibitors. <u>Bioorganic & Medicinal Chemistry</u> 15 (2007): 7865-7877.

[79]   Still, W. C., Tempczyk, A., Hawley, R. C. and Hendrickson, T. Semianalytical treatment of solvation for molecular mechanics and dynamics. Journal of the American Chemical Society 112 (1990): 6127-6129.

[80]   Miyamoto, S. and Kollman, P. Settle: An analytical version of the SHAKE and RATTLE algorithm for rigid water models. Journal of Computational Chemistry 13 (1992): 952-962.

[81]   Essmann, U., Perera, L., Berkowitz, M., Darden, T., Lee, H., et al. A smooth particle mesh Ewald method. The Journal of Chemical Physics 103 (1995): 8577-8593.

[82]   Tessier, M. B., DeMarco, M. L., Yongye, A. B. and Woods, R. J. Extension of the GLYCAM06 biomolecular force field to lipids, lipid bilayers and glycolipids. Molecular Simulation 34 (2008): 349-364.

[83]   J.CrystalSoft (2005-2006) Nanotube Modeler

[84]   Rungnim, C., Rungrotmongkol, T., Hannongbua, S. and Okumura, H. Replica exchange molecular dynamics simulation of chitosan for drug delivery system based on carbon nanotube. Journal of Molecular Graphics and Modelling 39 (2013): 183-192.

[85]   Rungnim, C., Arsawang, U., Rungrotmongkol, T. and Hannongbua, S. Molecular dynamics properties of varying amounts of the anticancer drug gemcitabine inside an open-ended single-walled carbon nanotube. Chemical Physics Letters 550 (2012): 99-103.

[86]   Ren, Y. P. and Pastorin, G. Incorporation of hexamethylmelamine inside capped carbon nanotubes. Advanced Materials 20 (2008): 2031-+.

[87]   Lee, E. C., Kim, D., Jurečka, P., Tarakeshwar, P., Hobza, P., et al. Understanding of Assembly Phenomena by Aromatic−Aromatic Interactions: Benzene Dimer and the Substituted Systems. The Journal of Physical Chemistry A 111 (2007): 3446-3457.

[88]   Janowski, T. and Pulay, P. High accuracy benchmark calculations on the benzene dimer potential energy surface. Chemical Physics Letters 447 (2007): 27-32.

[89]   Dapprich, S., Komáromi, I., Byun, K. S., Morokuma, K. and Frisch, M. J. A new ONIOM implementation in Gaussian98. Part I. The calculation of energies, gradients, vibrational frequencies and electric field derivatives. Journal of Molecular Structure: THEOCHEM 461–462 (1999): 1-21.

[90] Vreven, T., Morokuma, K., Farkas, Ö., Schlegel, H. B. and Frisch, M. J. Geometry optimization with QM/MM, ONIOM, and other combined methods. I. Microiterations and constraints. <u>Journal of Computational Chemistry</u> 24 (2003): 760-769.

[91] Tao, N. J. and Shi, Z. Monolayer Guanine and Adenine on Graphite in NaCl Solution: A Comparative STM and AFM Study. <u>The Journal of Physical Chemistry</u> 98 (1994): 1464-1471.

[92] Varghese, N., Mogera, U., Govindaraj, A., Das, A., Maiti, P. K., et al. Binding of DNA Nucleobases and Nucleosides with Graphene. <u>Chemphyschem</u> 10 (2009): 206-210.

[93] Hohenstein, E. G., Chill, S. T. and Sherrill, C. D. Assessment of the Performance of the M05−2X and M06−2X Exchange-Correlation Functionals for Noncovalent Interactions in Biomolecules. <u>Journal of Chemical Theory and Computation</u> 4 (2008): 1996-2000.

[94] Gowtham, S., Scheicher, R. H., Ahuja, R., Pandey, R. and Karna, S. P.Physisorption of nucleobases on graphene: Density-functional calculations. <u>Physical Review B</u> 76 (2007): 033401.

[95] Dalmark, M. Characteristics of doxorubicin transport in human red blood cells. <u>Scandinavian Journal of Clinical and Laboratory Investigation</u> 41 (1981): 633-639.

[96] Mignon, P., Loverix, S., Steyaert, J. and Geerlings, P. Influence of the π–π interaction on the hydrogen bonding capacity of stacked DNA/RNA bases. <u>Nucleic Acids Research</u> 33 (2005): 1779-1789.

[97] Kabsch, W. and Sander, C. Dictionary of protein secondary structure: pattern recognition of hydrogen-bonded and geometrical features. <u>Biopolymers</u> 22 (1983): 2577-2637.

[98] Richter, A., Drummond, D. R., MacGarvie, J., Puddicombe, S. M., Chamberlin, S. G., et al. Contribution of the Transforming Growth Factor B-loop - Sheet to Binding and Activation of the Epidermal Growth Factor Receptor. <u>Journal of Biological Chemistry</u> 270 (1995): 1612-1616.

[99] Yan, C., Pattani, V., Tunnell, J. W. and Ren, P. Temperature-induced unfolding of epidermal growth factor (EGF): Insight from molecular dynamics simulation. <u>Journal of Molecular Graphics and Modelling</u> 29 (2010): 2-12.

[100] Lee, D., Lockey, R. and Mohapatra, S. Folate receptor-mediated cancer cell specific gene delivery using folic acid-conjugated oligochitosans. <u>Journal of Nanoscience and Nanotechnology</u> 6 (2006): 2860-2866.

[101] Lemmon, M. A. Ligand-induced ErbB receptor dimerization. Experimental Cell Research 315 (2009): 638-648.

[102] Nunthaboot, N., Rungrotmongkol, T., Malaisree, M., Kaiyawet, N., Decha, P., et al. Evolution of Human Receptor Binding Affinity of H1N1 Hemagglutinins from 1918 to 2009 Pandemic Influenza A Virus. Journal of Chemical Information and Modeling 50 (2010): 1410-1417.

[103] Malaisree, M., Rungrotmongkol, T., Nunthaboot, N., Aruksakunwong, O., Intharathep, P., et al. Source of oseltamivir resistance in avian influenza H5N1 virus with the H274Y mutation. Amino Acids 37 (2009): 725-732.

VITA

<u>Personal information</u>

Name:	Chompoonut Rungnim
Date of birth:	23 June 1981
Address:	3/1 M.3 KohKret, Pak Kret, Nonthaburi, 11120, Thailand
e-mail:	chompoon.r@gmail.com

<u>Education</u>

2000 - 2003	B. Sc. in Chemistry (2nd Class Honours), Department of Chemistry, Faculty of Science, Chulalongkorn University, Thailand (GPAX 3.27)
2004 - 2005	M. Sc. in Petrochemical and Polymer Science, Faculty of Science, Chulalongkorn University, Thailand (GPAX 4.00)
2009 - 2012	Ph.D. in Nanoscience and Technology Program, Chulalongkorn University, Thailand (GPAX 4.00)

<u>Field of Research</u>

- Molecular dynamics simulation for the study of molecular interaction of carbon nanomaterials in biochemical application

- Quantum chemistry calculation of the interaction of guest molecule over carbon nanomaterials

<u>Publications</u>

1. C. Rungnim, U. Arsawang, T. Rungrotmongkol and S. Hannongbua "Molecular dynamics properties of varying amounts of the anti-cancer drug gemcitabine inside an open-ended single-walled carbon nanotube" Chemical Physics Letters, 550 (2012): p. 99-103.

2. C. Rungnim, T. Rungrotmongkol, S. Hannongbua and H. Okumura "Replica exchange molecular dynamics simulation of chitosan for drug delivery system based on carbon nanotube" Journal of Molecular Graphics and Modelling, 39 (2013): p. 183-192.